Materials & Design 254 (2025) 114106

Contents lists available at ScienceDirect

Materials & Design

journal homepage: www.elsevier.com/locate/matdes

Investigating EMI shielding performance of recycled polypropylene (PP) composite foams with reused metal powders

Valeria Marrocco [a], Rossella Surace [a,*], Elisabetta Brandonisio [a], Ilaria Marasco [b], Claudia Pagano [c], Cinzia Tonetti [d], Vito Errico [e], Giovanna Calò [b], Sabina L. Campanelli [e], Irene Fassi [c]

[a] CNR-STIIMA Institute of Intelligent Industrial Technologies and Systems for Advanced Manufacturing, Via P. Lembo 38F, 70124 Bari, Italy
[b] Politecnico di Bari, Department of Electric and Information Engineering, Via E. Orabona 4, 70126 Bari, Italy
[c] CNR-STIIMA Institute of Intelligent Industrial Technologies and Systems for Advanced Manufacturing, Via A. Corti 12, 20133 Milano, Italy
[d] CNR-STIIMA Institute of Intelligent Industrial Technologies and Systems for Advanced Manufacturing, Corso G. Pella 16, 13900 Biella, Italy
[e] Politecnico di Bari, Department of Mechanics, Mathematics and Management, Via E. Orabona 4, 70126 Bari, Italy

ARTICLE INFO

Keywords:
Recycled polymers
Reused metal powders
Foaming process
EMI shielding

ABSTRACT

Secondary raw materials, recycled Polypropylene (PP) and metal powders retrieved after use in the Powder Bed Fusion-Laser Beam process, are used to realize composite foams for microwave absorptance through chemical foaming. Morphological characterization allowed us to estimate foams' relative density, cell size, distribution, and circularity. The results highlighted that metal powders contributed to air cell nucleation during the process, thus influencing the final foam morphology. Then, numerical analyses were conducted on modeled PP foams to calculate Scattering (S) parameters and Shielding Effectiveness (SE), varying air cell areas, shapes, metal particle distribution, and evaluating their impacts on EM response. Based on simulation results, the S-parameters of all samples were then measured in the X-band. The calculated SE contributions, SE_R and SE_A, showed that foams with virgin and reused metal powders behave very similarly. Finally, four samples foamed from extruded pellets were characterized morphologically and electromagnetically. The outcomes showed extruded-based foams had a slightly decreased relative density, increased air cell numbers with lower circularity, and better uniformity in the air cell distributions. Confronting SE contributions in the X-band, SE_A improved by about 10%-20% compared to the mixed samples.

1. Introduction

Foams are cellular structures that have shown relevant suitability for electromagnetic interference (EMI) applications [1]. Indeed, their random porosity allows the electromagnetic (EM) waves to be almost fully entrapped within the structure, thus providing shielding effectiveness (SE) dominated by absorption and multiple internal reflections. At the same time, these structures can minimize secondary back reflection [2] and attain reduced EM pollution. To enable such a function, foams must be developed with specific materials simultaneously exhibiting electroconductivity and specific permittivity, i.e., a polymer matrix filled with electroconductive fillers. Recently, conductive polymer composites have been thoroughly investigated and proposed to develop absorption-dominated microwave shields [1–6]. In particular, the literature highlights a variety of composites that involve the use of diverse polymer matrices and electroconductive fillers. In this regard, thermoplastics, such as polylactic acid (PLA) [7–12], polypropylene (PP) [13–18], and polyethylene terephthalate (PET) [19], have been investigated. However, particular attention has been devoted to choosing the proper electroconductive material to enhance EMI shielding effectiveness (SE). Among them, carbon fibers (CF) [11,13], graphite carbon fibers (GCFs) [9,14], carbon nanotubes (CNTs) [10,19], graphene nanoplatelets (GNPs) [12], stainless steel fibers (SSFs) [15], and metal particles/powders (MPs) and oxides [16–18] were mainly evaluated.

Ameli et al. [15] evidenced that well-dispersed metal fibers in the PP

---

* Corresponding author.
E-mail addresses: valeria.marrocco@stiima.cnr.it (V. Marrocco), rossella.surace@stiima.cnr.it (R. Surace), elisabetta.brandonisio@stiima.cnr.it (E. Brandonisio), ilaria.marasco@poliba.it (I. Marasco), claudia.pagano@stiima.cnr.it (C. Pagano), cinzia.tonetti@stiima.cnr.it (C. Tonetti), vito.errico@poliba.it (V. Errico), giovanna.calo@poliba.it (G. Calò), sabinaluisa.campanelli@poliba.it (S.L. Campanelli), irene.fassi@stiima.cnr.it (I. Fassi).

https://doi.org/10.1016/j.matdes.2025.114106
Received 17 March 2025; Received in revised form 6 May 2025; Accepted 15 May 2025

matrix provided a large aspect ratio, reduced density of the composite, and reduction of the percolation threshold, leading to significant enhancement of the specific EMI SE (75 dB·g-1·cm^3). Agrawal et al. [16] focused on epoxy–PP composites filled with variable AlN particles prepared by the compression molding technique, unveiling that, with a maximum of AlN particle filler content (25 vol%), the PP-AlN composite significantly enhanced the thermal and dielectric characteristics compared to pure PP. Similarly, Zhou et al. [17] examined random PP copolymer (PP-R) samples with AlN nanoparticles fabricated through compression molding. The chemical and structural analyses were meant to characterize nanoparticle dispersion, DC conductivity, dielectric characteristics of the composite between 1 Hz-1 MHz, electrical breakdown, space charge distribution, thermal conductivity, and thermal stability to evaluate EMI shielding capability. Like the previous study in [16], the outcomes of the work in [17] highlighted that the thermal conductivity and stability increased with the filler content. Conversely, electrical properties worsen compared to pure PP, while the permittivity ($\varepsilon_r = 2.3–2.45$) and dielectric loss (<0.003) do not change significantly from 1 Hz to 1 MHz with variable filler contents. The dielectric characteristics at the GHz of a commercial low-loss PP with micro-ceramics and TiO_2 nanocrystals were investigated by Wilczyński et al. [18]. The numerical findings reported that the permittivity values underwent different variations by introducing ceramics or TiO_2 nanocrystals; in particular, adding ceramic nanoparticles to PP yields a higher permittivity increase (4.2) than TiO_2 (3.4). Conversely, grain shape, clustering, and dimensions of particles have a less significant impact on such a characteristic, while the particle aspect ratio affects the effective propagation constant and characteristic impedance. Although the metal fiber/powder inclusion in a thermoplastic can improve the composite's thermal and EMI characteristics, it is reasonable to expect that such fillers have a relevant drawback: costs. From this viewpoint, recycled/reused metal powders can be a solution. Therefore, to develop conductive polymer composite-based foams meant for microwave absorbers, the present article envisages deploying initial results concerning foams based on recycled PP supplied from industrial waste and filled with discarded metal powders retrieved from the metal additive manufacturing (MAM) processes.

Indeed, it is well acknowledged that MAM technologies generate a non-negligible amount of residuals that usually become waste. To cope with this issue, according to some Life Cycle Assessment (LCA) studies, wasted powders from the Powder Bed Fusion (PBF) technologies can be reused in the same processes, leading to cost reduction by about 40 % [20]. Practically, though, due to rigorous quality criteria imposed by some industrial applications, re-processing reused metal powders is essentially hindered or heavily subjected to the strict evaluation of the changes in the powders' characteristics after every process cycle [21]. During each building cycle, the powder is subjected to high temperatures and partial oxidation, causing changes in particle morphology, chemical composition, and flow characteristics. Therefore, after a certain number of manufacturing cycles, the powders were partially or completely substituted. Reusing materials discarded from MAM represents an opportunity to reduce material waste and its environmental impact. Therefore, assessing the suitability of exhausted metal powders from MAM as electroconductive fillers for producing EMI shielding foams will open a virtuous road and, at the same time, add a novel contribution to the current literature. In this work, virgin and reused metal powders (AISI316L and 17–4PH stainless steels, WC/Co/Cr-alloy, Ni-based superalloys) recovered by the Powder Bed Fusion-Laser Beam (PBF-LB) process [22] were considered as metal fillers in the recycled PP matrix. The foam samples realized for the present study encompassed two compositions: one was obtained by mixing the PP pellets, the metal powder, and the blowing agent in a solid state; the second procedure envisaged mixing extruded pellets made of PP/metal powder with the blowing agent. These two procedures were scheduled to evaluate if different metal powder dispersions may influence the foaming process, foam morphology, and final EMI SE performances. After the chemical foaming process, the samples were characterized by their morphology and EMI characteristics. In this regard, some numerical analyses are also proposed to support the discussion linking morphological data and EMI performance. A final investigation commented on foams' morphology and SE comparison between foams realized from mixed materials and those produced from extruded pellets.

2. Materials, preparation of conductive polymer composite

The polymer used in this study is a secondary raw material, the recycled PP resin provided by Recuperi Pugliesi Srl. This material is retrieved by transforming various industrial wastes, such as agricultural sheeting, plastic foil, and packaging, into extruded pellets after washing them with a biological purifier. The recycled PP follows the standard UNI 10667–3: 2011 and has a purity of 98 %, density of 0.94 kg/dm^3, Vicat softening temperature of 90 °C, and pellet size of 13 mm. Referring to metal powders, stainless steels (AISI316L and 17–4PH), WC/Cr/Co alloy, and Ni-based superalloys are recovered from PBF-LB resources (virgin) and discards (reused). The AISI 316L and 17–4PH powders are supplied by Mimete Metal Powders, whereas WC/Cr/Co-alloy and the (Ni)–based superalloy powders were provided by MBN Nanomaterialia S.p.a. and LPW Technology, respectively. In their virgin state, all powder types exhibit a spherical shape induced by the gas atomization process, which is essential for ensuring optimal flowability and packing density during the PBF-LB process. The particle size distribution for these powders ranges between 15 μm and 45 μm. However, increased reuse cycles induced particle chemical and shape modifications [20–27]. In [28], Zhuo et al. demonstrated by SEM observation that the repeated reuse of Ti6Al4V powders resulted in decreased satellite particle formation and increased particle deformation with diminished sphericity after 12 cycles. Furthermore, the surface of the particles becomes rougher, and some agglomerated and fractured particles are present. Li et al. [29] evidenced that powder reuse had various effects on Particle Size Distribution – PSD depending on the materials. For example, the PSD of 17-4PH after 10–20 building cycles notably widened [30], while a slightly wider size distribution was observed for AISI316L after thirty cycles [31]. The authors in [32] observed that AISI316L particle morphology alterations due to repeated PBF-LB processing could significantly affect the flowability and packing density of the powders, thus causing problems, especially during the recoating stage. Similarly, Li et al. [33] pointed out that NiTi powder alloys experienced a slight shift in distribution towards an extensive particle size range and increased oxygen content.

Fig. 1 shows the SEM images of virgin and re-used powders: the AISI316L powder virgin and reused 20 and 50 cycles (Fig. 1a-b-c, respectively) and the Ni-based superalloy powder virgin and reused 2 cycles (Fig. 1d-e). As is inferable from Fig. 1, reused powders exhibit some deformed or elongated particles, along with satellite particle formation. In this regard, it can also be observed that some particles feature lower minimum dimensions (minimum diameter equal to 7.6 μm) than those measured in the virgin state. The SEM images of metal powders also showed the presence of oxidation spots and layers partly covering the metal particles, although their thicknesses are very thin, around nanometers, after several reuse cycles, as confirmed by the literature [34].

EDS compositional analyses were also performed, and the element % wt content average and standard deviation are reported in

Table 1. The AISI 316L types show different content of Fe, Cr, Ni, Mn, Mo, Si, and O, while Ni-based superalloy metal powders present Ni, Cr, Co, Ti, Al, Mo, W, and O. In particular, the compositional analyses evidence that the powders, especially the reused ones, featured reduced wt % of oxygen content, indicating a restrained oxidation process. It must be highlighted that for AISI 316 L powder, having 20 cycles of reuse, some of the different analyzed quantities exhibited significant variability in the Cr (1.03 ± 0.11), Ni (19.85 ± 0.33), and Mo (3.66 ± 0.17) contents, which, as shown in the subsequent Sections, affected the

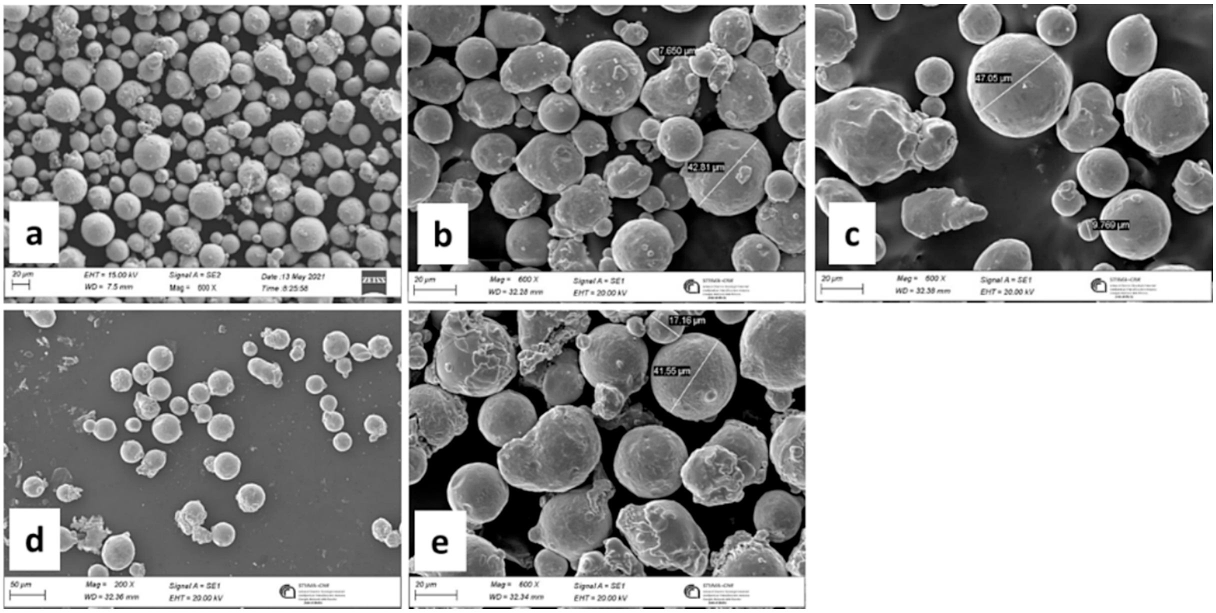

Fig. 1. SEM images of (a) – (b) – (c) AISI316L stainless steel powder virgin and reused 20 and 50 cycles, respectively, (d) – (e) Ni-based superalloy powder virgin and reused 2 cycles.

Table 1
EDS of AISI 316L virgin, reused for 20 and 50 cycles, EDS of Ni-based superalloy powder, virgin, and reused for 2 cycles.

% wt content	AISI316L virgin	AISI316L_20	AISI316L_50	Ni virgin	Ni_2
O	1.09 ± 0.29	0.65 ± 0.3	1.38 ± 0.30	0.38 ± 0.29	0.10 ± 0.16
Si	0.57 ± 0.11	0.99 ± 0.11	0.52 ± 0.11	–	–
Cr	18.91 ± 0.26	18.57 ± 0.26	18.77 ± 0.31	15.75 ± 0.22	15.46 ± 0.21
Mn	1.40 ± 0.20	1.66 ± 0.2	2.25 ± 0.25	–	–
Fe	63.08 ± 0.43	64.24 ± 0.43	65.14 ± 0.49	–	–
Ni	13.34 ± 0.33	12.63 ± 0.32	10.83 ± 0.37	56.49 ± 0.38	58.83 ± 0.35
Mo	1.59 ± 0.16	1.26 ± 0.16	1.09 ± 0.16	2.82 ± 0.15	2.36 ± 0.15
Al	–	–	–	4.4 ± 0.14	3.98 ± 0.14
Ti	–	–	–	7.14 ± 0.15	6.19 ± 0.15
Co	–	–	–	10.13 ± 0.24	10.49 ± 0.24
W	–	–	–	2.92 ± 0.16	2.58 ± 0.15

Table 2
Composition of foams realized with PP and metal powders.

Sample n.	Polymer	CBA 1 wt%	Metal powder 10 wt%	Reusing cycles
0	Recycled PP	ADC	/	/
1			AISI316L Stainless steel	virgin
2				20
3				50
4			17–4 PH Stainless steel	virgin
5				10
6			WC/Co/Cr alloy	virgin
7				10
8			Ni-based superalloy	virgin
9				2

foaming process.

2.1. Chemical foaming process

To produce thermoplastic polymer-based foams, physical foaming involving CO_2 in supercritical conditions (sc-foaming) [6,7,19], injection molding [9,13,15], chemical foaming [11], CNC milling [12], compression molding [16,17] can be employed to attain specific foam density, cell size and shape ensuring targeted SE. This work exploited chemical foaming to produce electroconductive foams based on recycled PP and metal powders. To this aim, ten precursors were prepared by preserving the mass proportion of materials. In the first (sample 0), PP pellets were mixed with the foaming agent (CBA) in the proportion of 1 % of the total PP weight (wt%); then, in other samples, 10 % wt of metal powder was added to the PP/CBA solid mix. The mixed samples' number and composition are shown in Table 2, emphasizing the number of cycles of metal powder reuse.

To further investigate the foaming process and performance of the composites, four additional precursors were prepared mixing PP and metal particles using a mini extruder with a screw with length and diameter equal to 230 mm or 16 mm, respectively. Considering the screw's short length, the polymer matrix (recycled PP) and the metal fillers (SEM analyses on extruded pellets used to prepare samples 2ex and 4ex are shown in Fig. 2: the images unveil the presence of isolated and very small metal particles (MPs) distributed within the polymer matrix is particularly evident.

Table 3) were fed simultaneously in the throat of the extruder, respecting the desired proportion (10 wt% of fillers). Due to the moderate quantity of material available, small portions of the components (1 g ± 0.01 g in total) were prepared and fed into the extruder in a series to improve the dispersion of the fillers. The material feeding frequency was set according to the resident time of the extrusion (20 s) calculated from preliminary experiments using recycled PP. Finally, to attain the homogeneity of the mixing, the extruded material was pelletized and re-extruded with the same process parameters: screw speed 20 RPM and feeder, compression, and metering zone temperatures equal to 160°C, 180°C, and 190°C respectively. The obtained composites were then mixed with CBA (1 wt%). SEM analyses on extruded pellets used to prepare samples 2ex and 4ex are shown in Fig. 2: the images unveil the presence of isolated and very small metal particles (MPs) distributed

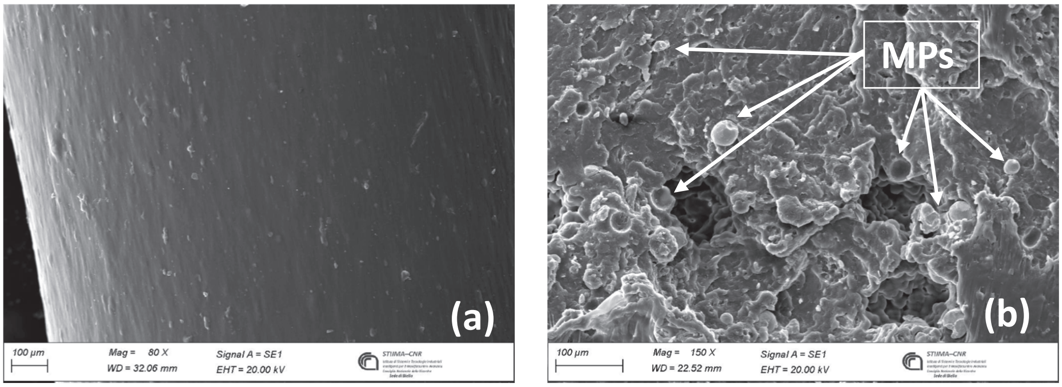

External surface Section

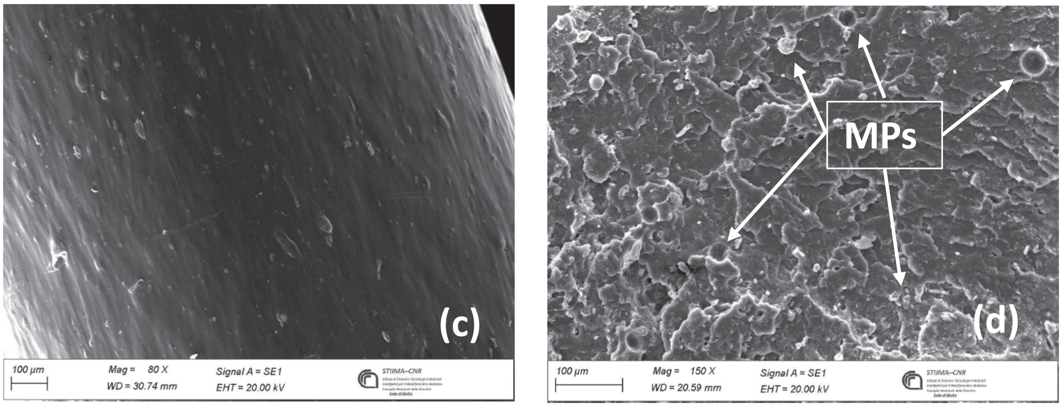

External surface Section

Fig. 2. SEM images of (a) external surface and (b) section for the extruded pellets made of PP + AISI 316 L reused for 50 cycles used for sample 2ex preparation; SEM images of (c) external surface and (b) section for the extruded pellets made of PP + Ni-based superalloy reused for 2 cycles used for sample 4ex preparation.

Table 3
Foam composition based on extruded PP with AISI 316L and PP with Ni-based superalloy.

Sample n.	Polymer	CBA 1 wt%	Metal powder 10 wt%	Reusing cycles
1ex	Recycled PP	ADC	AISI316L Stainless steel	20
2ex				50
3ex			Ni-based superalloy	virgin
4ex				2

within the polymer matrix is particularly evident.

The PP/CBA/metal powder solid precursor was placed into an open silicon mold and into a pre-heated electric furnace (Memmert Excellent 400) to initiate chemical foaming. For this study, the samples underwent a temperature of T = 190°C (foaming temperature) for t = 105 min (foaming time). These process parameters were set based on previous tests. The chemical foaming process encompasses three phases: cell formation, growth, and stabilization. Due to the temperature rising, the polymer melts, and the CBA decomposes, producing a gas, which induces the polymer/gas mixture growth and the cell formation. In order to promote cell growth, the chemical CBA decomposition temperature must fall within the same range as the polymer blend's melting temperature. For this reason, Azodicarbamide – ADC by Acros Organics (purity of 97 %) is chosen as a CBA exothermic agent without any additional modifier or accelerator. ADC decomposes around 200-220°C [35] and generates gas, mainly nitrogen, and small amounts of carbon dioxide, carbon monoxide, and ammonia. The cell growth is the most critical phase of the process, and, as such, temperature fluctuations must be controlled to preserve the thermodynamically unstable liquid state of the foam and avoid coalescence. This phenomenon may induce an increase in the cell's diameter, a decrease in cell number, and a change in the relative density, which may affect the final EMI shielding performance [5,6,11]. Finally, the foams were cooled by applying air to stabilize the structure and prevent the foam's cells from collapsing.

3. Morphological characterization: Results and discussion

The foams' morphology was first measured with a digital caliper to assess the total volume after expansion; then, all samples were sawed cut longitudinally (Fig. 3) with a diamond blade to evaluate the shape and dimensions of air cells. The cross-sections of one-half of the foams were acquired with a 3D optical profilometer (Sensofar S Neox) (Fig. 4) and then processed visually via image analysis software (ImageJ) to

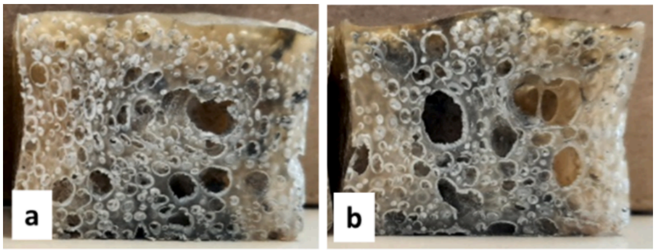

Fig. 3. Cross-section of some obtained samples: a) n. 1 (AISI316L virgin), and b) n. 5 (17–4-PH reused 10).

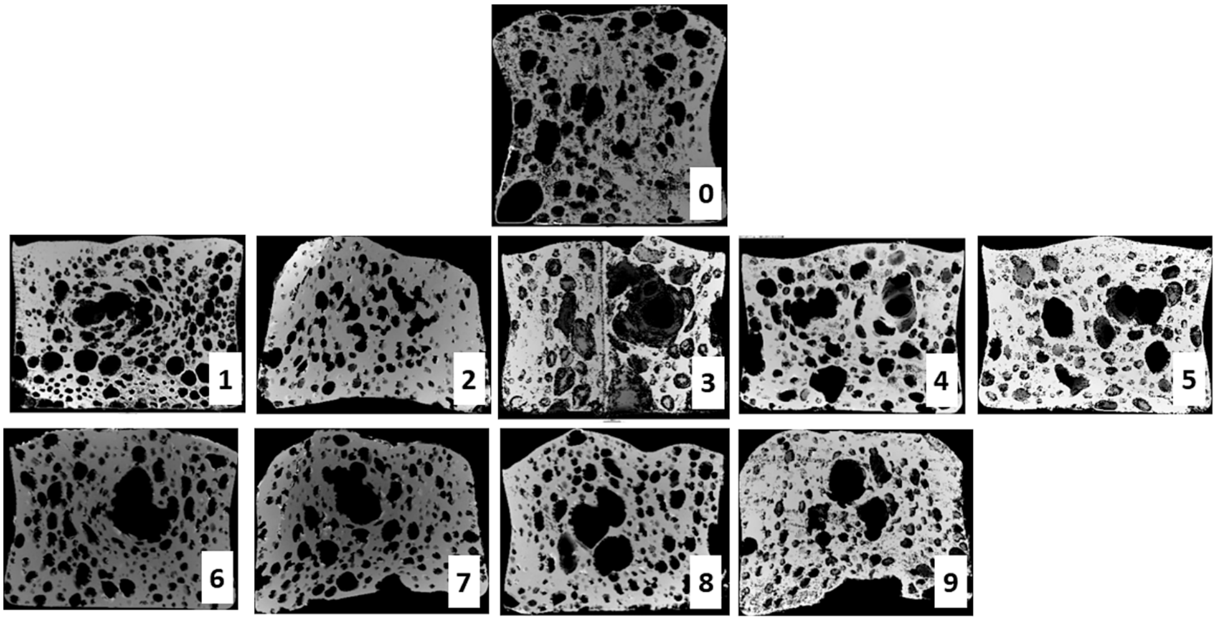

Fig. 4. Optical images of samples' cross-section (sample numbers in Table 2).

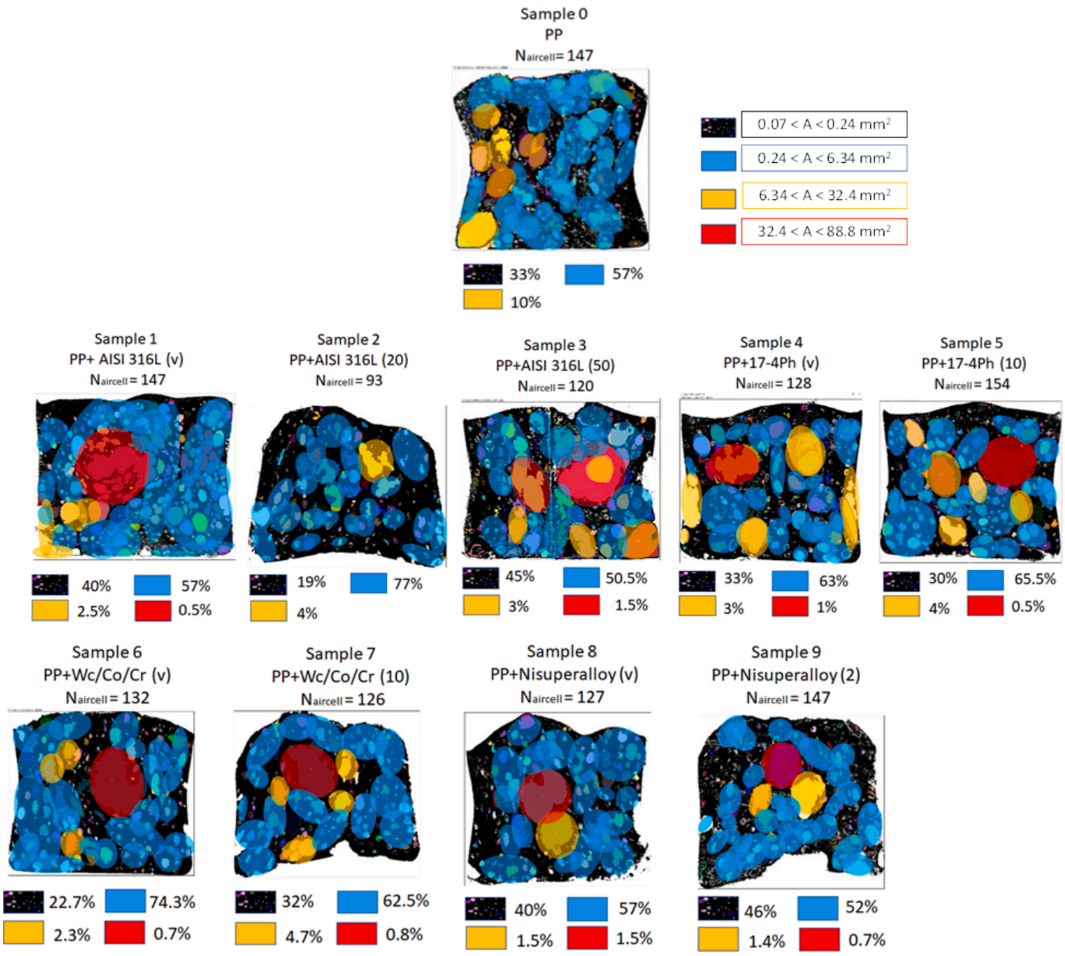

Fig. 5. Cell area distribution: the portion of the cross-sections is colored depending on the air cell dimension: dots on a black background identify small pores; cyan indicates surfaces displaying medium cells, and yellow and red superimpose the larger and giant pores. (For interpretation of the references to colour in this figure legend, the reader is referred to the web version of this article.)

extrapolate the cell number and areas.

Among morphological parameters [28], the most relevant is the relative density, defined as the ratio of foam density and material density. The structure's weight, homogeneity, and isotropy can be estimated by cell density, cell area distribution, and circularity. In particular, cell density is defined as the ratio of the counted cell number in a frame of the acquired area; this operation allows for uniformity of the results, independent of the actual cross-section sizes. The measured cell areas are then aggregated by calculating their median value, representing the midpoint value of the frequency distribution of observed areas, and dividing the number of observations by two, such that there is an equal probability of pores falling above or below it. Finally, the circularity parameter C is expressed as $C = 4\pi A/P^2$, where A and P are the cells' area and perimeter, respectively; if $C = 1$, perfect spherical cells can be observed; conversely, $C < 1$ indicates an ellipsoidal shape. For all samples, the results for the described parameters are summarized in

A visual technique is exploited to highlight the different cell dimensions and distributions in each sample (Fig. 5). In particular, dots in the black background within the cross-section represent the surface portion, including smaller cells; the cyan zones indicate the areas with medium cells, while yellow and red zones correspond to large and giant air cells, respectively. The area dimension ranges and respective colors are specified at the bottom of Fig. 5. Each figure also reports the percentage of air cells for each area dimension range over the entire cross-section area. The upper caption of each subfigure describes the sample number, composition, and the total number of air cells counted in the cross-section.

Sample 0 is the reference recycled PP foam without metal powders: as inferable from the images and the data, pure PP foam shows a homogenous distribution of air cells, mostly small (black dotted zones in Fig. 5) and medium (cyan), which appear mainly elongated along the longitudinal axis. Samples 1, 2, and 3, i.e., PP foams with AISI316L powders, feature a different morphology depending on the quality of the metal particles. For instance, including virgin AISI316L powder in the PP (sample 1) induced the formation of more cells (147 in the cross-section), larger cell density, and circularity than the other two samples, n.2 and 3 (Table 4). However, when the AISI316L reused for 20 cycles was mixed in the PP (sample 2), the foaming process did not yield similar results, leading to reduced cell number (93), smaller cell areas (more medium cells), and increased relative density (Table 4). Nonetheless, when the foam involving AISI 316L 50 is examined (sample 3), it can be found that the cell number increases (120), although less than sample 1, leading to lower relative density. Additionally, this sample shows the formation of two giant cells (red zone, Fig. 5), mainly located in the upper half of the cross-section and surrounded by medium pores (cyan zones in Fig. 5). Comparing results for AISI316L powders suggests that virgin and reused powders affect cell formation differently. The peculiar case of sample 2 might also be due to the variability of elements stressed in the EDS analyses, especially the decreased content of Cr and increased Ni and Mo, which compose the powder. In the case of PP foams mixed with 17-4PH (samples 4 and 5), the morphology does not display a significant difference considering virgin or reused powders, except for the total number of air cells, which increases when reused 17-4PH is mixed with PP. Additionally, both foams show large and giant merged cells surrounded by smaller and medium ones, which, also in these cases, can be localized in the upper half of the inspected surfaces. These characteristics are also found in samples 6, 7, 8, and 9, i.e., PP foams mixed with WC/Co/Cr and Ni-superalloy-based powders, independently of their reuse cycles.

Table 4
Morphological characterization: relative density, cell density, cell area distribution median, and circularity parameter.

Sample n.	Relative density	Cell density (cells/cm^2)	Cell area distribution median (mm^2)	Circularity parameter
0	0.40	16.35	0.51	0.146
1	0.38	27.33	0.53	0.390
2	0.45	10.76	0.60	0.329
3	0.40	8.11	0.36	0.219
4	0.38	14.17	0.40	0.180
5	0.38	17.18	0.61	0.201
6	0.37	14.66	0.57	0.342
7	0.41	13.46	0.58	0.345
8	0.35	13.14	0.51	0.273
9	0.39	16.94	0.37	0.179

As is noticeable, the main discrepancy in all samples can be found in the air cell area and distribution. Generally, including virgin powders (samples 1, 4, 6, and 8) promotes medium air cell growth (cyan zone) and produces less dense foams. In contrast, reused powders allow cell size heterogeneity, favoring smaller and medium pores (dots in black background) associated with forming one or two giant cells (Table 4). Concerning spatial distribution, the formation of the giant (red zone) and large (yellow zone) pores occurs more prominently in foams produced using reused powders. In this regard, neglecting samples 0 and 2, all remaining foams show the presence of one or two central giant bubbles (red zones) and a few larger cells (yellow zones). These peculiar features could be attributed to PP's properties and the effect of metal powders during the foaming process. In fact, despite its excellent chemical, physical, and mechanical properties, such as high thermal and corrosion resistance, specific strength, hardness, and high fatigue strength, PP has a weak melt strength, making it difficult to be foamed compared to other plastics. In particular, if the melt strength is too weak, the cell walls separating the bubbles are not strong enough to bear the extensional force, which causes the bubbles to agglomerate and break [36]. Additionally, it must be considered that the set foaming temperature (190°C) suitable for ADC decomposition, is slightly higher than the melting point of the PP (about 160°C). This temperature value, associated with PP's low viscosity, can lead to the formation of larger cells and, often, cell coalescence [37]. Researchers have proposed certain techniques to overcome these disadvantages, encompassing organic and inorganic fillers, fibers, and nanoparticles [38]. Besides, in the present study, adding metallic powders contributes to nucleation along with the products deriving from the decomposition of the CBA, thus boosting gas bubble formation. Therefore, the number of nuclei and the nucleation rate are also determined by the distribution of the metal particles within the polymer melt and by the polymer melt surface tension. As a result, the foaming system originates from a heterogeneous nucleation process, where the energy barrier of the bubbles is much smaller than that of a homogeneous system, and leads to larger cell dimensions. It must be underlined that the polymer's thermal conductivity is morphology-dependent: this characteristic is boosted by a crystalline domain and oppositely reduced by the amorphous one. Due to its low crystal density [39], PP is mainly amorphous and has low thermal conductivity (0.12 W/mK), which could be detrimental to the foaming process. Nonetheless, the metallic fillers increase the composite's thermal conductivity [40], and consequently, the heat transfer in the sample thanks to their high coefficients (for example, stainless steel has 17 W/mK) [41]; in this regard, also filler size, shape, orientation, and arrangements can contribute to improving this characteristic [42]. Hence, the foaming process differs depending on the metal particle type (virgin or reused) and characteristics. Regarding electrical conductivity, improving the material's conductivity can simultaneously improve the SE in absorption and reflection, promoting the material's EMI shielding performance [43]. For example, the electrical conductivities at 20°C of some of the used fillers are (S/m) 1.45x106 for stainless steel [44]. These values should theoretically ensure better absorption for the composite foams due to increased losses.

4. Scattering parameters (S-parameters) and shielding effectiveness (SE) of the mixed conductive composite foams

4.1. *Numerical analysis: Estimating S-parameters and SE performance in PP foams with variable air cell areas and shape*

A coaxial probe 85070C connected to a Vector Network Analyzer (VNA – Agilent Technologies, N9917A) was first used to characterize the pure PP bulk and foam's relative complex permittivity $\varepsilon = \varepsilon_r\text{-}j\varepsilon_i$, in the frequency range between 0–2.5 GHz. To account for the morphological anisotropy, the PP foam's relative permittivity was measured in two directions, i.e., the foam growth and the transversal one. Both PP bulk and foam displayed almost constant average permittivity values throughout the frequency range: the bulk PP has $\varepsilon_r = \sim 2$ and $\varepsilon_i = 0.008$, while pure PP foam shows very close values in both directions, $\varepsilon_r = 1.2\text{–}1.3$ and $\varepsilon_i \sim 0$, indicating an approximately isotropic and lossless foam. Reasonably, the average real permittivity of the foam is lowered compared to the bulk PP due to increased air fraction, which benefits the impedance matching and the consequent reduction of secondary reflections. The bulk permittivity of the PP foam was then used to perform numerical analyses via CST Microwave Studio. To this aim, a foam model sizing 2x2x1.6 cm^3 and encompassing a bulk structure with random spatially distributed ellipsoidal pores was implemented; real and imaginary permittivity were obtained by measurements interpolation over an extended frequency range, 0.5–14 GHz, which allowed for a broader evaluation of S-parameters and SE response. The total air cell number was equal to 300, while air cell areas ranged between 0.07 mm^2 and 6.34 mm^2, as indicated by the morphological characterization. The air cells were built in a developed MATLAB routine that considers cell size ranges retrieved from morphology analyses; the routine allows the introduction of shape deformation, i.e., axial factor in all planes, enabling the spherical air cells to be stretched properly along x, y, and z directions. The simulations considered an EM plane wave at normal incidence and an E-field output monitor located perpendicularly to the propagation direction in near-field conditions. The analyses were conducted to estimate S-parameters, which were then used to calculate SE contributions, i.e., absorption involving multiple internal reflection contributions (SE$_A$) and reflection (SE$_R$), according to the following formulas (1–2-3) [11]:

$$SE = SE_R + SE_A \tag{1}$$

$$SE_R = 10log_{10}\left|\frac{1}{1-R}\right|,\ R = \left|{S_{11}}^2\right| \tag{2}$$

$$SE_A = 10log_{10}\left|\frac{1-R}{T}\right|,\ T = \left|{S_{21}}^2\right| \tag{3}$$

Fig. 6a-c-e shows the S-parameter trends calculated by increasing the maximum equivalent value of the air cell radius and decreasing its ellipsoidal ratio. For simplicity in the discussion, we refer to the xy plane

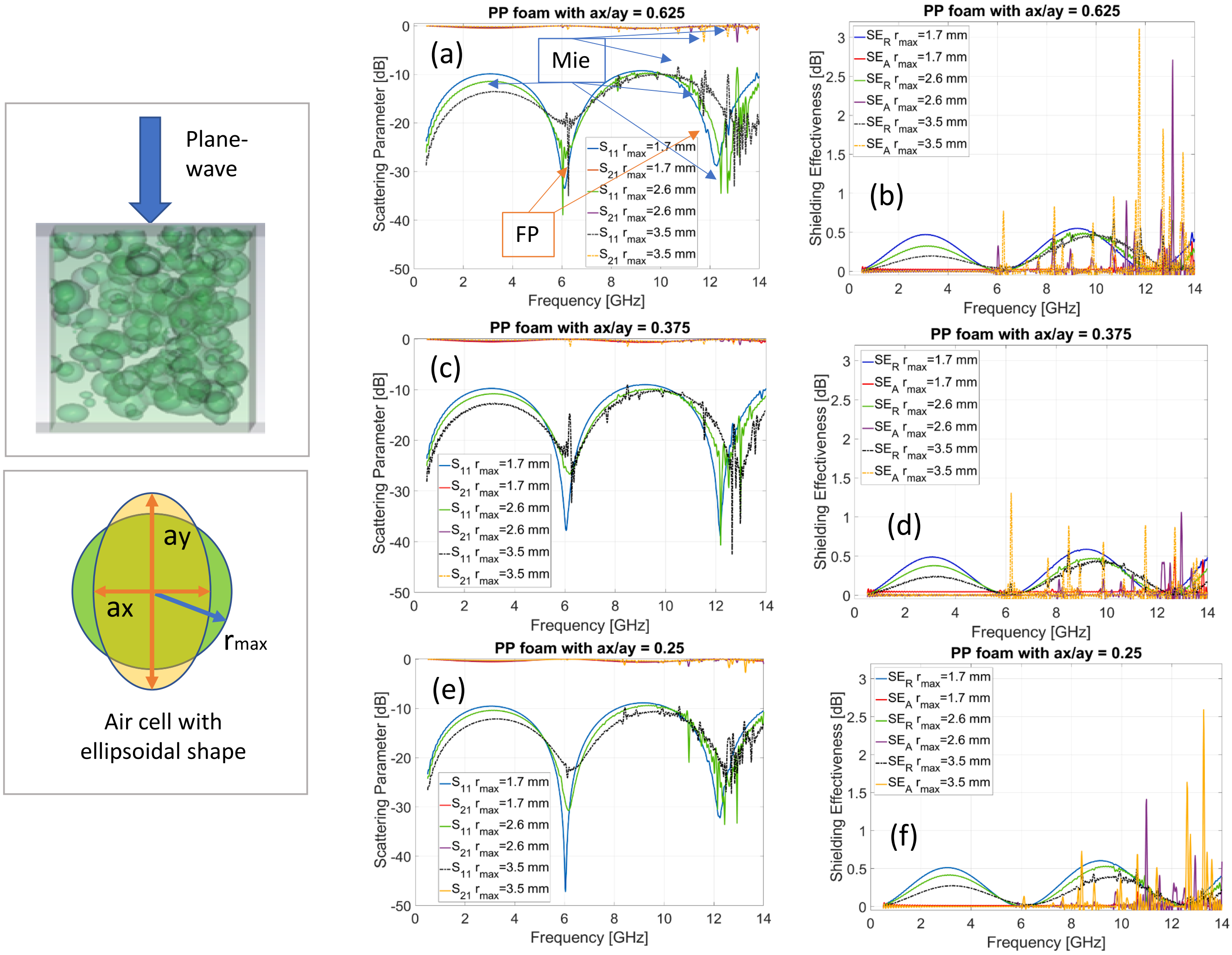

Fig. 6. (a) – (c)- (e) Scattering Parameters and (b) – (d) – (f) SE$_R$ and SE$_A$ of PP foams, calculated by varying air cell sizes and ellipsoidal ratio (ax/ay). The simulated foams have 300 randomly distributed air cells.

axial factor (ax/ay). When the EM plane wave impinges on a finite dielectric structure, resonant modes called Fabry-Perot (FP) originate within the structure; these resonances are identified by pronounced dips in the S_{11} trend and lighter peaks in the S_{21}. The frequencies at which these modes occur depend on the structure's effective permittivity (involving the bulk permittivity, air fraction included in the bulk, and finite dimensions of the structure). As visible from Fig. 6a-c-e, when the maximum equivalent air cell radius is increased, the air fraction introduced in the polymer induces a decrease in the structure's effective permittivity, which leads to FP modes shifting towards higher frequencies. At the same time, air cells enable multiple internal scattering since the EM field is reflected and transmitted back and forth within the foam due to the refractive index contrast at the polymer/air cell inner interfaces. When the refractive index contrast is high enough, part of the EM field remains entrapped in the air cells, giving rise to Mie resonances [11,45]. Such modes are typically characterized by lower intensity and smaller width than FP modes (Fig. 6a-c-e), and, due to their nature, they occur when the air cell size is much smaller than the impinging EM wavelength. In the proposed numerical investigation, the areas of the ideal spherical air cells have equivalent radii ranging between 0.17 mm and 3.5 mm, corresponding to wavelength values λ/20, being $\lambda = \lambda 0/\mathrm{sqrt}(\varepsilon\mu)$, λ0 the minimum free-space wavelength, ε and μ the permittivity and permeability of the structure, respectively. Considering such characteristics, Mie resonances can be appreciated at higher frequencies, especially after 6 GHz, as evidenced in the S_{11} and S_{21} plots of Fig. 6a-c-e f. Regarding SE contributions, it can be noticed from Fig. 6 b-d-f that the SE_R trends follow FP modes behavior, and, independently of the air cell sizes or shape, the maxima do not surpass 0.5 dB; these low values of SE_R indicate good impedance matching and almost complete EM field penetration in the structure. Differently, SE_A trends exhibit high sensitivity to cell size and shape, as EM absorptance is mainly due to Mie resonances, which are responsible for entrapment of the EM field within the foam. In this regard, when the area of air pores grows, several peaks appear reasonably at lower frequencies. Moreover, it can be noticed that the ellipsoidal ratio (ax/ay) impacts the resonance intensity and slightly affects the frequency. It can be underlined that the ellipsoidal cell shape and orientation cannot be controlled during the random distribution construction. Therefore, since the EM plane wave excitation is set at the normal incidence, this random air cell orientation might lead to underestimating the SE_A compared to the real foam's SE performance.

Likewise, the PP foam model with MPs was built using a MATLAB-developed routine that allows the introduction of air cells and metal particles, and enables their dimension variation, shape deformation along x, y, and z directions, i.e., axial factors (fixed at 0.625). The cell size ranges were set based on the morphology observed in the experiments, taking into account the analyzed cell nucleation of the different metal particles. The whole structure is 20 mm x 20 mm x 16 mm, which is intended to equal half of the average sample size. Also in this case, the simulations were performed considering a plane wave incident EM field, which allows estimating a broader frequency range (8–14 GHz). The simulations evaluated the S-parameters for different metal particle/cluster distributions, i.e., randomly distributed in the foam and more gathered in the center, keeping their number/volume identical in each simulation (approximately 10 % of the volume). SE_R and SE_A were then calculated using S-parameters. For synthesis, the SE plots and E-field distributions at specific frequencies of foams encompassing PP with Steel and PP with Nickel metal particles are reported in Fig. 7, where the type of resonances concerning specific scattering phenomenon (air cells internal reflections and metal particle scattering) are also highlighted. In particular, it can be observed that when multiple internal reflections (MIRs) occur due to Mie resonances, SE_R is minimized, and SE_A is maximized. Conversely, SE_R and SE_A are simultaneously enhanced when the metal particles induce reflection/scattering within the structure. It can be noticed that internal reflection caused by metal particles is generally and reasonably more intense than multiple internal reflections caused by polymer/air discontinuity due to air cells. Moreover, depending on the clusters and air cell sizes, these scattering phenomena can happen simultaneously at some frequencies, ending in total SE ($SE_R + SE_A$) enhancement compared to PP foam without metal particles. Finally, the simulations show that distributing the same quantity of metal particles differently within the porous structure impacts its EM reflection and absorptance capability. In particular, localized metal particles perform better than distributed ones, especially for Steel. This behavior is due to the mirror-like effect, which enhances the scattering phenomena more than distributed metal particles.

4.2. SE performance of recycled PP foams with virgin metal powders

Following the indication provided by simulation results, the foams' S-parameters in the X-band were measured via WR90 transitions connected to the Vector Network Analyzer (VNA – Agilent Technologies, N9917A), operating between 0–18 GHz (Fig. 8). Initially, all measurements were performed by cutting half of each sample into smaller pieces matching the WR90 sizes. Undesirably, for all samples, the results superimposed the PP response. This lack of variation was ascribed to the significant modification of the air-cell morphology and metal particle

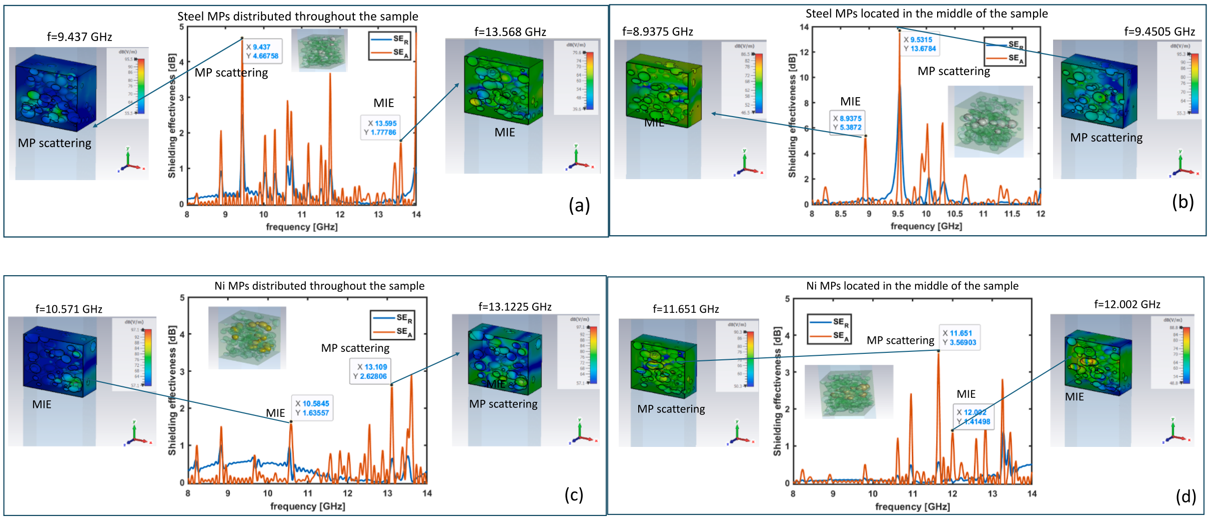

Fig. 7. SE_R and SE_A of PP foam with Steel 1010 MPs, (a) distributed throughout the sample, (b) located in the middle; SE_R and SE_A of PP foam with Ni MPs, (c) distributed throughout the sample, (d) located in the middle.

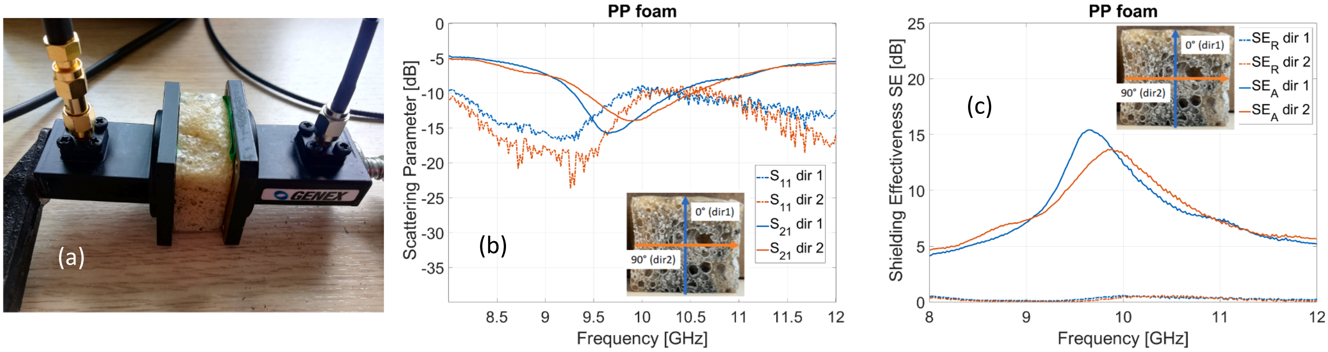

Fig. 8. (a) PP-Foam sample sandwiched between WR90 transitions connected to the VNA by SMAs, (b) Scattering parameters S_{11} (red curve) and S_{21} (blue curve) of neat PP; (c) SE_A and SE_R for direction 1(blue solid and dashed curves) and 2 (red solid and dashed curves) and) of neat PP. Sample orientations used for measurements are: 0° refers to the foam growth direction (dir 1), and 90° sample orientation refers to the transversal direction (dir 2). (For interpretation of the references to colour in this figure legend, the reader is referred to the web version of this article.)

loss induced by the cut. Therefore, as shown in Fig. 8a, we measured the other half of the sample portion (about 3.6x3.6x1.6 cm^3) utilizing a resonant cavity method, in which the sample is sandwiched between the two WR90 waveguides. For all samples, double S-parameters measurements were done, considering two sample orientations (insets in Fig. 8): the first was carried out considering the incidence of the WG mode normal to the cross-section oriented at 0° (foam growth direction, dir 1), and the second measurement was performed by rotating the sample of 90° (transversal direction, dir 2). This procedure accounted for air cell orientation and non-homogeneous metal powder distribution within the electroconductive foams (SEM images in Section 5).

Fig. 8 b-c depicts the recycled PP foam's S-parameters, SE_A, and SE_R contributions, which were calculated from S_{11} and S_{21} measurements using the formulas reported in the previous section [11]. As inferred from the plots, PP foam displays minor reflective shielding ($SE_R < 0.5$ dB) due to the low value of ε_r. Since the PP has no dielectric losses, it is also expected to have a small SE_A. Instead, the PP foam exhibits good absorptance capability. Indeed, the main peak falls at the FP resonance

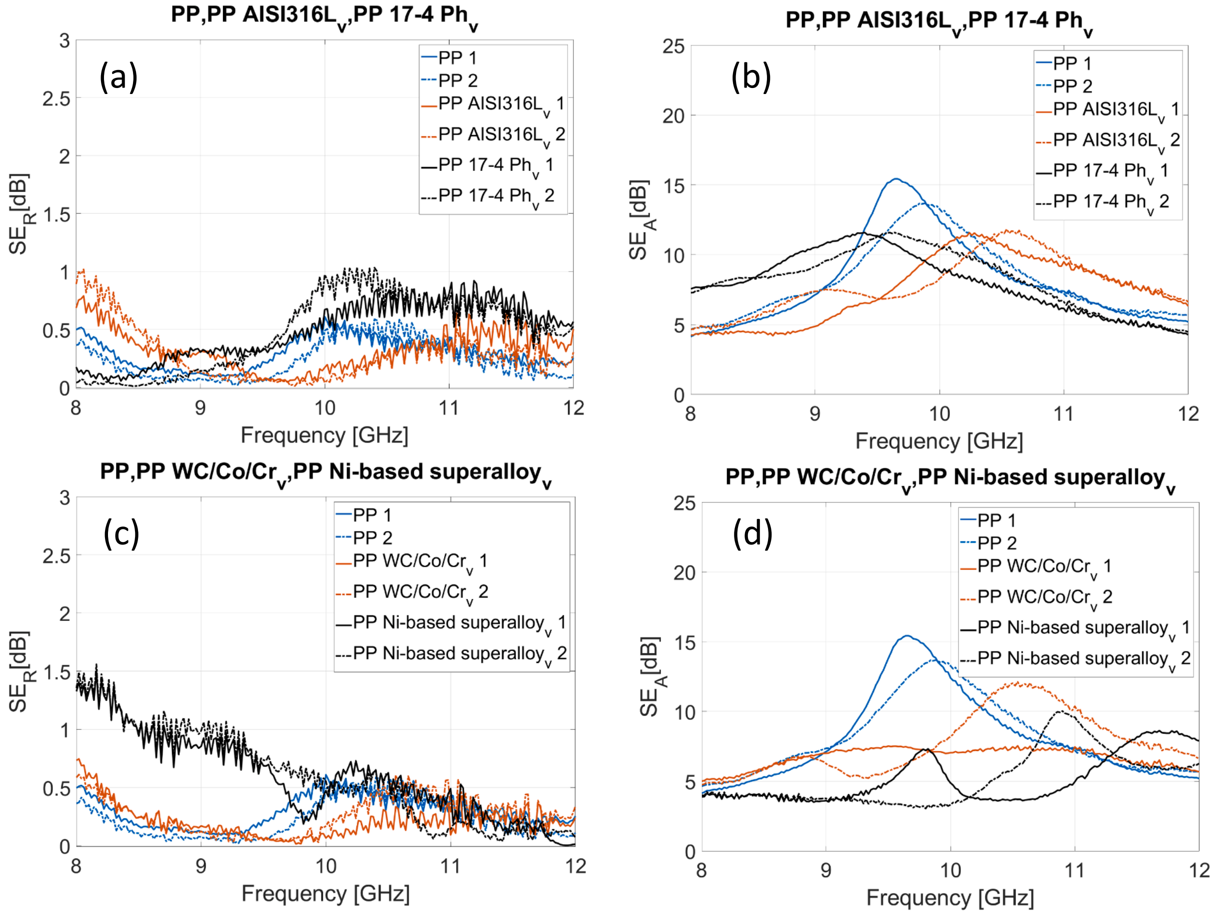

Fig. 9. (a) SE_R and (b) SE_A of PP (blue lines), PP with AISI316L (red lines) and 17-4PH (black lines) virgin powders foams; (c) SE_R and (d) SE_A of PP (blue lines), PP with WC/Co/Cr (red lines) and Ni-superalloy-based (black lines) reused powders foams. The solid lines refer to direction 1 (sample orientation 0°); dashed-dotted lines direction 2 (sample orientation 90°). (For interpretation of the references to colour in this figure legend, the reader is referred to the web version of this article.)

frequency, whose position is mainly determined by the sample thickness. As visible, the resonance slightly shifts depending on the measurement direction due to anisotropy: 9.7 GHz for direction 1 (blue line in Fig. 8c) and 9.9 GHz for direction 2 (red line in Fig. 8c). Also, the predominance of medium air cells (median areas of 0.51 mm^2) allows multiple internal scattering phenomena in the X-band; however, as noticed by the simulations, cell elongation and orientations affect MIRs' contributions to SEA and cause the slight shift of the peak position according to the measurement directions.

Fig. 9 depicts the SE$_R$ and SE$_A$ of all samples realized considering the inclusion of virgin metal powders in the PP-based composite. Fig. 9 a- c show that SE$_R$s have very low values, below 1.5 dB, demonstrating that the EM field mainly penetrates the foams in every case. It is worth noticing that metal particles increase the SE$_R$ (~1dB) compared to PP foam, as observed in the simulations. However, the effect of different foam morphology and metal powder inclusion emerges evidently in the SE$_A$. In all Fig. 9, SE$_A$ maxima of the samples cannot be found at close frequencies since the measured half-samples have different thicknesses (Table 5). At the same time, the peak intensity is determined by the relative densities, air cell size, number, and distribution. Additionally, likewise sample 0, in the following cases, the absorption peak can be slightly shifted, depending on the measurement direction.

Considering the PP with AISI316L (sample 1) and 17-4PH powders (sample 4) foams plotted in Fig. 9b, it can be observed that the absorption maxima in the two measurement orientations are found at very close frequencies – at 10.3 GHz and 10.5 GHz for sample 1 and at 9.3 GHz, and 9.6 GHz, for sample 4 – and with same intensities (11.5 dB). As is inferable, the SEA curves exhibit a similar trend (wideband). In this regard, Table 5 shows that samples have different thickness ($t = 1.74$ cm for sample 1 and $t = 1.92$ cm for sample 4), which explains the different maxima positions; at the same time considering the relative density (Table 5), air cell densities and median distribution areas ($\rho r = 0.44$, 27.33 cell/cm^2, 0.53 mm^3 for sample 1 and $\rho r = 0.37$,14.17 cell/cm^2, 0.40 mm^2 for sample 4) justify the curve widening and the slight maxima shift according the measurement direction. Increasing thickness would shift the FP resonance to a lower frequency at a fixed relative density. Conversely, decreasing thickness would lead to a higher frequency shift. Moreover, sample 4 has a lower relative density and cell density than sample 1, and these factors imply a decrease in the effective permittivity that induces FP resonance to broaden and move slightly at higher frequencies. Inconveniently, the low SE$_A$ intensity exhibited by both samples suggests that multiple internal scattering and reflections induced by metal particles give a lower contribution.

Finally, Fig. 9d plots the SE$_A$s for PP with WC/Co/Cr (sample 6) and Ni-superalloy-based (sample 8) virgin powders. The curves highlight that PP with virgin WC/Co/Cr (red solid line) has an almost flat response in the 0° measurement direction (dir 1). This sample has $t = 1.64$ cm, $\rho r = 0.34$, which involves the broadening of the FP peak induced by a low effective permittivity of the half-foam. Furthermore, as inferred from Fig. 5, the air cell distribution disclosed a significant percentage of small and medium air cells, and the presence of a giant air cell in the sample elongated in the foam growth direction. Therefore, when the WG90 mode impinges on the cross-section, it passes through with negligible interaction with the first layers. Indeed, considering the area of the giant cell, the resonance is expected at frequencies around 1.2 GHz. Furthermore, as the mode propagates in the sample, the air cells with smaller areas enable multiple internal scattering at very high frequencies, whose resonances can also be detected beyond the X-band. As a result, the absorption in the X-band is reduced. Rotating the sample changes the effective permittivity of the cross-section encountered by the WG90 mode. In this case, the effect of the giant cell is reduced, while small and medium air cells become more engaged. This leads to better EM interaction with the porosity, which entails better SE$_A$, as witnessed by a satisfactory absorption (10.2 dB) at 10.6 GHz. Half foams with PP and Ni-based superalloy (sample 8) have t = 1.29 cm, ρr = 0.36, which implies a large FP mode at a higher frequency. Observing the plots, inadequate performance (below 10 dB) can be observed in the frequency range of interest for 0° measurements, although two small peaks appear at 9.8 GHz and 11.8 GHz. In this case, the first peak at 9.8 GHz is likely ascribed to multiple internal reflections occurring in medium cells, while the second is the FP resonance. In contrast, a peak displaying 10 dB at 11 GHz appears when the measurement is performed at 90°, suggesting the combined effect of FP mode and multiple internal reflections. Since the samples 6 and 8 are characterized by very small relative density or thickness, cell densities can add details on how EM absorption is accomplished: sample 6 has 13.14 cells/cm^2 and privileged the presence of medium/large cells, which can enable multiple internal reflection in the X-band; conversely, sample 8 has higher cell density (16.94 cells/cm^2), but also significantly smaller air pores, including one giant air cell (Fig. 5), that hints at relevant EM absorption outside the X-band.

Table 5
Density, thickness and relative density of the measured half samples.

Sample	Polymer/ MPs	Type of MPs	Half sample Density ρ (cm^3/g)	Thickness t (cm)	Half sample Relative Density ρr
0	PP		0.4	1.64	0.42
1	AISI 316L	virgin	0.45	1.74	0.44
2	AISI 316L	20	0.46	1.47	0.45
3	AISI 316L	50	0.39	1.53	0.38
4	17–4 PH	virgin	0.39	1.92	0.37
5	17–4 PH	10	0.38	1.75	0.37
6	WC/Co/Cr	virgin	0.35	1.66	0.34
7	WC/Co/Cr	10	0.41	1.86	0.4
8	Ni-based	virgin	0.37	1.26	0.36
9	Ni-based	2	0.4	1.53	0.39
1ex	AISI 316L	20	0.39	1.65	0.37
2ex	AISI 316L	50	0.32	1.68	0.33
3ex	Ni-based	virgin	0.37	1.80	0.36
4ex	Ni-based	2	0.33	1.84	0.34

4.3. *SE performance of mixed foams made of recycled PP with reused metal powders from PBF-LB*

Fig. 10a-c shows the SE$_R$ and SE$_A$ plots for the PP with AISI 316L metal powder, referring to measurements performed in the transversal direction 1 at 0° (solid lines) and direction 2 at 90° (dotted lines). As clearly visible, these foams also present very low shielding by reflection, ranging between 0.5–1 dB. Conversely, absorption provides more details as their trends vary depending on the half-foam thickness and morphology. As already noticed, PP foam with virgin AISI 316L displays higher cell density than pure PP, improving the interaction between the EM field and the foams and, consequently, the SE$_A$. When the PP foam with AISI316L reused 20 (sample 2) is investigated, the SE$_A$ exhibits two peaks measured for direction 1 (red solid line) at 9.08 GHz and 11 GHz, featuring very low absorption (7 dB and 9.8 dB, respectively). Considering the other sample orientation (red dash-dotted line), the foam has two SE$_A$ absorption resonances at 9.6 GHz and 11.6 GHz, characterized by SE$_{Amax}$ = 8.6 dB and SE$_{Amax}$ = 13.6 dB, respectively. The morphology data (Table 5) for sample 2 report $t = 1.47$ cm, $\rho r = 0.45$; therefore, it has a slightly higher relative density than sample 1, but significantly smaller thickness, determining an effective permittivity decrease compared to PP with virgin AISI316L (sample 1) that causes the FP to shift towards higher frequency. Additionally, sample 2 is characterized by fewer cells, mainly displaying small and medium areas, which yield improved internal EM scattering at higher frequencies, leading to better SE$_A$. In this regard, a higher SE$_A$ intensity has been measured in direction 2, suggesting that air cell orientation and metal particle dispersion interact more efficiently with the EM field in this direction. Conversely, PP foam enriched with AISI316L reused over 50 times (sample 3) shows acceptable SE$_{Amax}$ = 10.4 dB at 10.4 GHz (black solid line) in direction 1

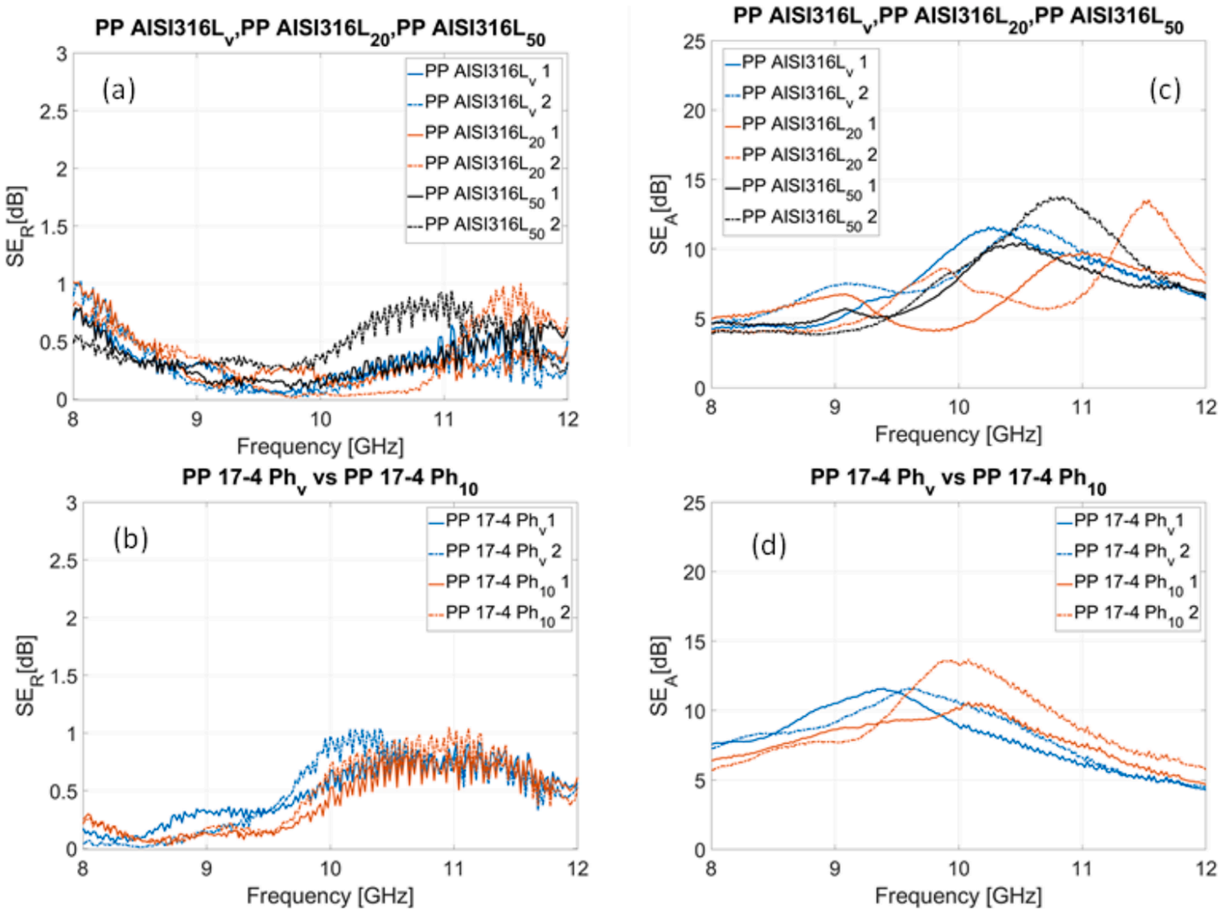

Fig. 10. (a) SE_R and (b) SE_A PP and virgin (blue lines) and reused (red and black lines) AISI316L powders foams; (c) SE_R and (d) SE_A of PP and virgin (blue lines) and reused 17-4PH powders (red lines) foams. The solid lines refer to direction 1 (sample orientation 0°); dashed-dotted lines indicate direction 2 (sample orientation 90°). (For interpretation of the references to colour in this figure legend, the reader is referred to the web version of this article.)

and good $SE_{Amax} = 13.7$ dB at 11.8 GHz in direction 2. Sample 3 exhibits a $t = 1.53$ cm, lower relative density ($\rho r = 0.38$) than samples 1 and 2, as evidenced by larger and giant air pores in the cross-section. Hence, this foam has a lower effective permittivity than sample 1 and higher than sample 2, which moves the FP resonances between samples 1 and 2. Moreover, thanks to an almost equal distribution of small and medium air cells, multiple internal scattering is improved after 10 GHz. As a result, the SE_A is enhanced for the combined effect of FP and Mie resonances and scattering by metal particles.

SE_R and SE_A of samples 4 and 5 (PP with virgin and reused 17–4 PH stainless steel) are plotted in Fig. 10c-d. As clearly noticeable, sample 5 with PP and reused 17–4 PH powders shows a relevant SE_A enhancement for both directions (red solid and dashed lines in Fig. 10d) compared to sample 4 involving virgin powder. However, the maxima are right-shifted at around 10.1 GHz. Inspecting morphological data and Table 5 may explain the slight diversities: samples 4 and 5 have the same relative density (ρr = 0.37), but different thickness (t = 1.92 cm, for sample 4, t = 1.75 cm, for sample 5). As previously described, by fixing the relative density, the reduced thickness causes the shift of PF towards higher frequency. Comparing cell numbers per area (14.17 cell/cm^2 for sample 4 and 17.18 cell/cm^2 for sample 5), distribution, and sizes (0.4 mm^2 and 0.61 mm^2, respectively) provides insights on the peak intensity: from Fig. 5 it can be appreciated that sample 4 mainly has small and medium cells, while sample 5 features more air cells of medium dimensions, which allows the EM fields to interact efficiently especially with the porosity at higher frequencies in direction 2.

The SE_R and the SE_A of samples 6 and 7 – PP foams with WC/Cr/Co powders- are shown in Fig. 11a-b. As already appreciated in the other samples, SE_R still ranges between 0.5 dB and 1 dB. Analyzing SE_A incisively illustrates various responses, especially depending on the sample orientation. Focusing on sample 6, the measurements along 0° (blue solid lines) show an almost flat SE_A behavior characterized by an average value of 7 dB throughout the whole range, while sufficient absorption of 10.2 dB is appreciated at 10.6 GHz for 90° measurements. Sample 7 follows an opposite trend: indeed, higher SE_A (maximum of 12 dB) is obtained around 9.7 GHz for 0° measurement (red solid line), while the same SE contribution in the transversal direction is reduced and flattened (10 dB) at the same frequency (red dashed-dotted line). Sample 7 is characterized by t = 1.86 cm, slightly larger than sample 6, so FP was expected to shift to a lower frequency. However, samples 6 and 7 have dissimilar relative densities (0.34 for sample 6 and 0.4 for sample 7). So, the latter exhibits higher effective permittivity, which improves the SE_A intensity by shrinking the curve; finally, the larger percentage of small air cells shown by the PP foam with reused WC/Cr/Co powders compared to the virgin counterpart aids the EM field entrapment, which is also boosted by metal particles scattering, further contributing to the SE_A intensity.

Finally, the results of PP with Ni-based superalloys (samples 8 and 9) are compared in Fig. 11c-d. The SE_R in Fig. 11c exhibits slightly higher values (1.5 dB for sample 8 and 1 dB for sample 9) at the first edge of the frequency range, while inspecting SE_A plots in Fig. 11d uncovers insufficient efficiency. As already discussed, the foam with virgin Ni-based superalloy powder (blue lines) showed poor absorptance capability in the X-band, independently of the sample orientation. Conversely, although the foam with Ni-based superalloys reused 2 (sample 9) reports low SE_A values for 0° orientation, improved shielding by absorption (a

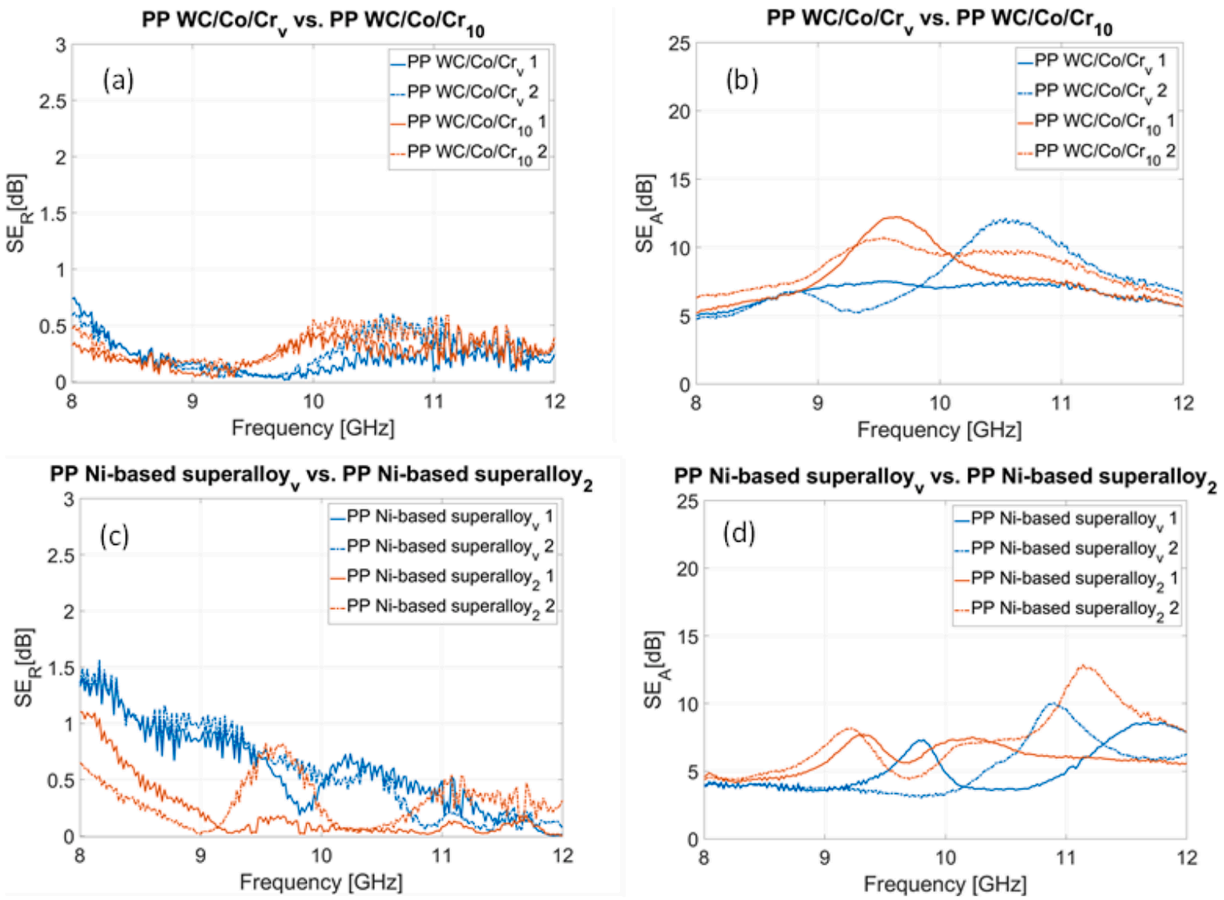

Fig. 11. (a) SE_R and (b) SE_A of PP and virgin (blue lines) and reused (red lines) WC/Co/Cr powders foams; (c) SE_R and (d) SE_A of PP and virgin (blue lines) and reused Ni-based superalloy (red lines) powders foams. The solid lines refer to direction 1 (sample orientation 0°); dashed-dotted lines indicate direction 2 (sample orientation 90°). (For interpretation of the references to colour in this figure legend, the reader is referred to the web version of this article.)

peak of 13 dB is recorded at 11.1 GHz) is observed when the sample is rotated by 90°. In this regard, sample 9 has $t = 1.53$ cm and a relative density of 0.39; this enables the PF to shift at a lower frequency and shrink due to an increased effective permittivity, which benefits the SE_A peak compared to sample 8. Furthermore, sample 9 has more cells and a significantly lower median cell area distribution (0.37 mm^2), which allows for a more efficient multiple internal scattering than sample 8.

Table 6
Comparison of morphological parameters between extruded- and mixed-based foams: relative density, cell density, cell area distribution median, and circularity parameter.

Sample n.	Relative density	Cell density (cells/cm^2)	Cell area distribution median (mm^2)	Circularity Parameter
Ext/Mixed	Ext/Mixed	Ext/Mixed	Ext/Mixed	Ext/Mixed
1ex/2	0.36/0.45	18.14/10.76	0.69/0.60	0.176/0.329
2ex/3	0.32/0.40	17.61/8.11	0.65/0.36	0.239/0.219
3ex/8	0.35/0.35	21.94/13.14	0.53/0.51	0.140/0.273
4ex/9	0.33/0.39	18.30/16.94	0.92/0.37	0.197/0.179

5. Morphology and SE comparison between mixed-material and extruded-material-based foams

To further investigate the foaming process and SE performance, four additional samples, foamed starting from composite pellets obtained by the extrusion of PP and metal particles, were produced and characterized (Table 6, Fig. 12). The indicators describing foam morphology reported in Table 6 and the visual inspection of air cell area distribution (Fig. 12) show that the cell density and area distribution in the extruded samples increase compared to mixed samples. Moreover, Fig. 12 also shows that, similarly to sample 2 (Fig. 5), sample 1ex preserves the absence of giant cells and a predominance of smaller/medium cells. Similarly, the graphic air cell distributions of sample 3 in Fig. 5 and sample 2ex in Fig. 12 show the formation of an almost equal number of medium and smaller pores. Concerning PP foams with Ni-based superalloy (3ex and 4ex), a similar scenario can be observed: in particular, compared to their mixed counterparts, air cells with medium areas increase, while the percentage of smaller ones decreases. Confronting the graphical cell distributions of samples 3ex and 4ex (Fig. 12) with samples 8 and 9 (Fig. 5) reveals additional morphological similarities concerning the dimension and position of the large air cells, mainly formed in the foam center. The extrusion facilitates the formation of medium cells, as their percentage in almost every extruded sample is higher than in the corresponding mixed sample. In summary, extruded-based composite foams display improved foam morphology. In this regard, it can be assumed that a more homogeneous dispersion of metal particles promotes more controlled and homogeneous cell growth, as underlined in Section 3. However, to verify this, SEM analyses were performed on the samples 3 and 2ex, PP + AISI 316L 50 mixed- and extruded-based

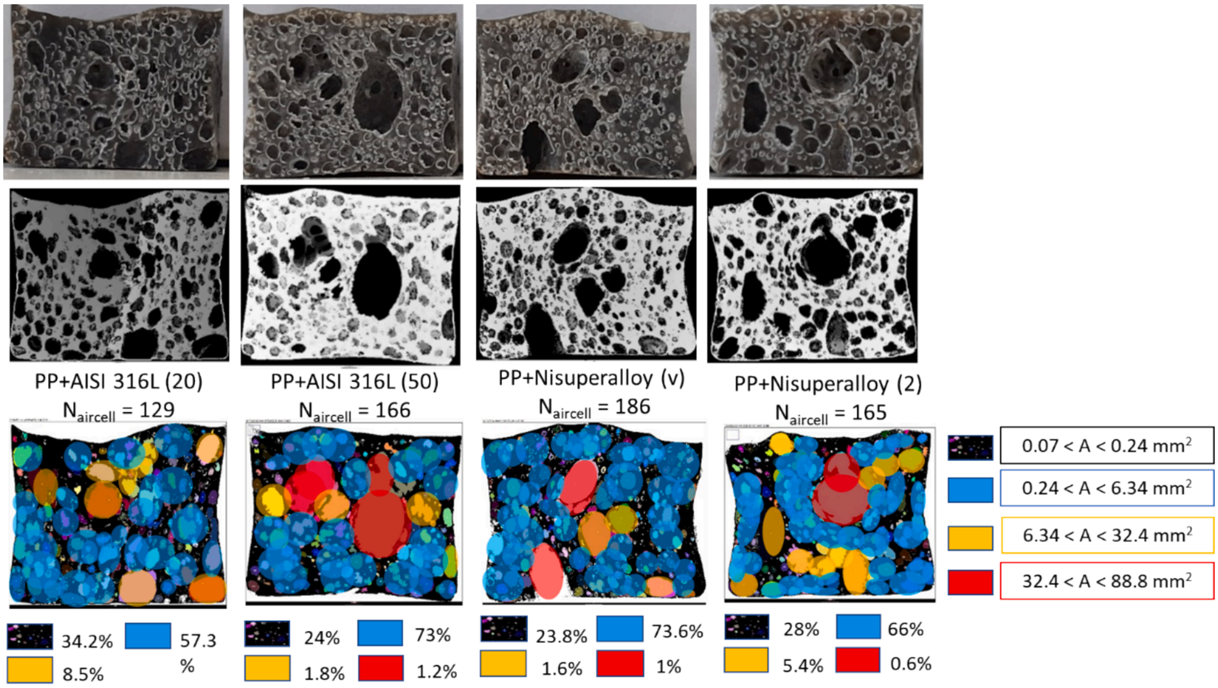

Fig. 12. Cross-section, optical images, and air cell area distribution of the foam samples made from extruded pellets. The cross-sections are colored depending on the cell areas: dots in a black background identify small pores; cyan indicates surfaces displaying medium cells, and yellow and red superimpose the larger and giant pores. (For interpretation of the references to colour in this figure legend, the reader is referred to the web version of this article.)

foams, respectively, and samples 9 and 4ex, PP + Ni-based superalloy 2, mixed- and extruded-based foams, respectively. Some metal particles/clusters (indicated with MPs) are visible in the following figures. Although the examined regions are limited, the images indicate more distributed MPs in the extruded foams than their mixed counterparts, which display more isolated particles. As a result, extruded-based foams, including metal powders, exhibit, on average, lower relative densities and greater cell density and area distribution. However, the circularity parameter follows an inverse trend compared to mixed samples: using virgin metal particles or metal particles with reduced cycles of reuse yields higher circularity for mixed samples. Conversely, higher circularity is found for reused metal particles in the extruded-based foams. See (Fig. 13).

Fig. 14 report the SE_R and SE_A performance of the extruded-based foams compared to the mixed-material-based ones (samples 2, 3, 8, 9): as visible in Fig. 14a, the SE_R results to be further decreased using extruded pellets, likely due to better metal particle dispersion and less relative densities of the foams which involve better impedance matching. As noticeable from Fig. 14b, extruded-based foam with PP and AISI316L reused 20 times (blue lines) shows higher SE_A for 0° sample orientation than the mixed counterpart: indeed, the extruded-based foam displays a peak of 13 dB similar to the mixed foam, but at a

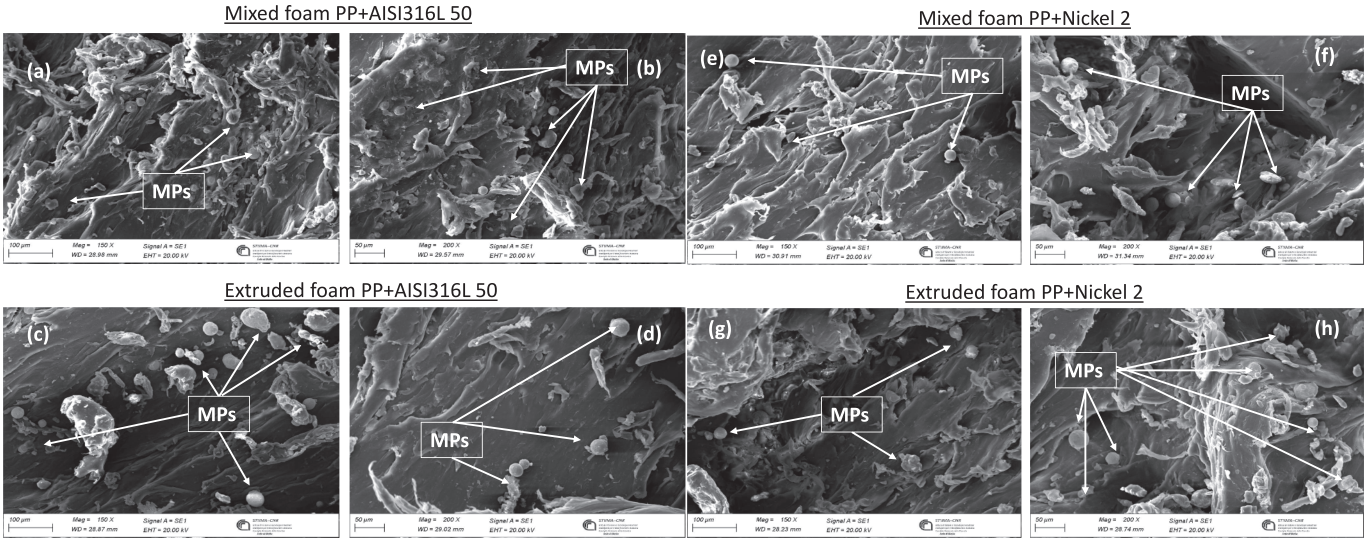

Fig. 13. SEM images in different zones of the composite foams at different magnification and in different areas: (a) 150X and (b) 200X magnification of the mixed-based PP + AISI 316L 50 foam (sample 3); (c) 150X and (d) 200X magnification of the extruded-based PP + AISI 316L 50 foam (sample 2ex); (e) 150X and (f) 200X magnification of mixed-based PP + Ni-based superalloy 2 foam (sample 9); (g) 150X and (h) 200X magnification of extruded-based PP + Ni-based superalloy 2 foam (sample 4ex).

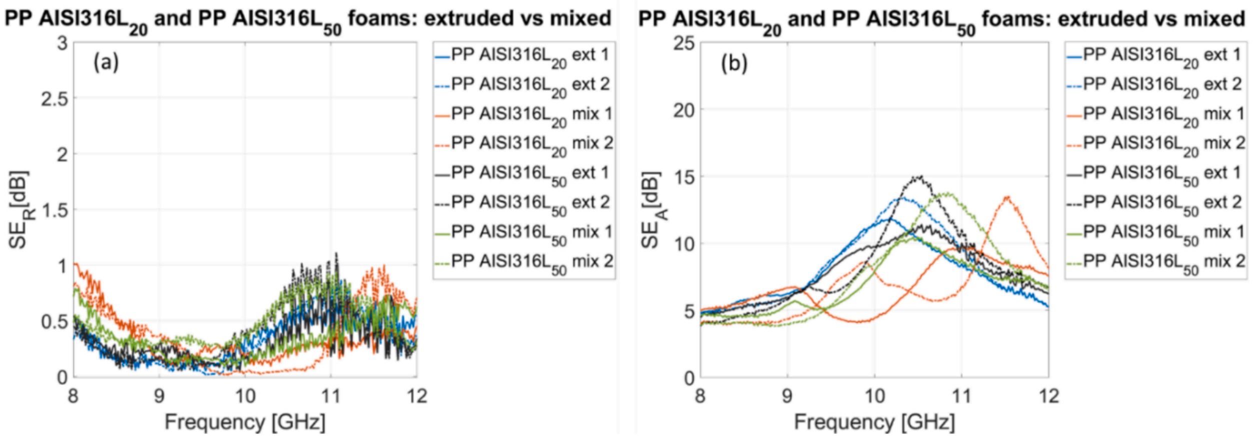

Fig. 14. (a) SE$_R$ and (b) SE$_A$ of foams obtained by extruded and mixed PP with AISI316L reused for 20 and 50 cycles.

lower frequency of 10.1 GHz. Sample 1ex has a higher thickness (t = 1.65 cm, Table 5) than sample 2, and so, the peak is shifted at a lower frequency; this foam also has a significantly lower relative density (ρr = 0.37, Table 5) than sample 2, which tends to decrease the effective permittivity, broadening the resonance and decreasing the SE$_A$ maximum. Conversely, similar values of SE$_A$ are found for both samples at 90° orientation, although at reasonably different frequencies. The maximum intensities measured in the extruded-based sample 1ex are due to the dimensions of the medium air cells, which exhibit wider areas than those in sample 2, involving multiple internal scattering and EM field entrapment to occur at lower frequencies. Similar behavior can be identified for sample 2ex (black lines in Fig. 14) compared to sample 3 (green lines in Fig. 14). The extruded PP with AISI 316L 50 foam has a t = 1.68 cm, slightly larger than the mixed counterpart, which explains the SE$_A$ slight peak shift, a lower relative density (0.33) than sample 3, resulting in the widening of the peak. Nonetheless, it exhibits higher maxima than sample 3, reasonably attributed to multiple internal reflections and scattering occurring efficiently around the FP mode and leading to SE$_A$ enhancement. Also, direction 2 promotes better shielding by absorption for such foams, likely due to cell orientation and elongation.

Regarding foams with Ni-based superalloys, SE$_R$ settles below 1 dB, except for the X-band lower edge (Fig. 15a). SE$_A$ trends reported in Fig. 15b unveil that extruded-based samples slightly improve the absorbance in both directions compared to mixed foams. It must be noticed that samples 3ex and 4ex have similar thicknesses (in Table 5, 1.84 cm and 1.86 cm, respectively). Therefore, their FP resonances are closer and fall in the X-band; additionally, the multiple internal scattering is effective considering the cell density and distributions of the samples. Furthermore, considering the measurement direction, SE$_A$ peaks occur at close frequencies, especially in reused Ni-superalloy-based powder, hinting at an almost isotropic response. Despite this, SE$_A$ peaks do not display particularly high values, as lower relative densities (0.36 and 0.33) give these samples a wideband SE$_A$ behavior rather than a selective one.

Generally, the results show that extruding composite pellets can benefit the morphology, particularly the foam density, cell dimensions, and homogeneity of cell distribution, but not the circularity compared to mixed-based samples: indeed, remarkable ellipsoidal shapes characterize virgin particle-based extruded foams. However, the highest SE$_A$ is measured for sample 2ex, which exhibits the highest circularity value among the extruded-based samples, particularly along 90°orientation (black dashed lines in Fig. 14b). Still, sample 4ex, which has the second highest C value, has a slightly lower SE$_A$ peak in direction 2 (black dashed line in Fig. 15b) than sample 1ex (blue dashed line in Fig. 14b).

Finally, since all half samples hardly have the same densities and thickness, Specific SE (SSE = avSE/ρ [dB/g/cm^3]) and Absolute Specific SE (aSSE=SSE/t [dB/g/cm^2]) were calculated and reported in Fig. 16 to assess the actual total shielding effectiveness in the X-band. The average SE equals the total SE (SE$_R$ + SE$_A$) values averaged throughout the X-band and then divided by the sample relative density ρ to obtain SSE; aSSE is calculated considering SSE divided by the thickness t of each measured half sample. As inferred from the following histograms, the specific SSE and absolute aSSE in direction 2 are the most promising for the final application in the X-band. Furthermore, regarding the metal particle type and the metal particle inclusion method, extruded-based, especially concerning AISI316L 50 and Ni 2, demonstrated improved SSE and aSSE compared to the mixed counterparts.

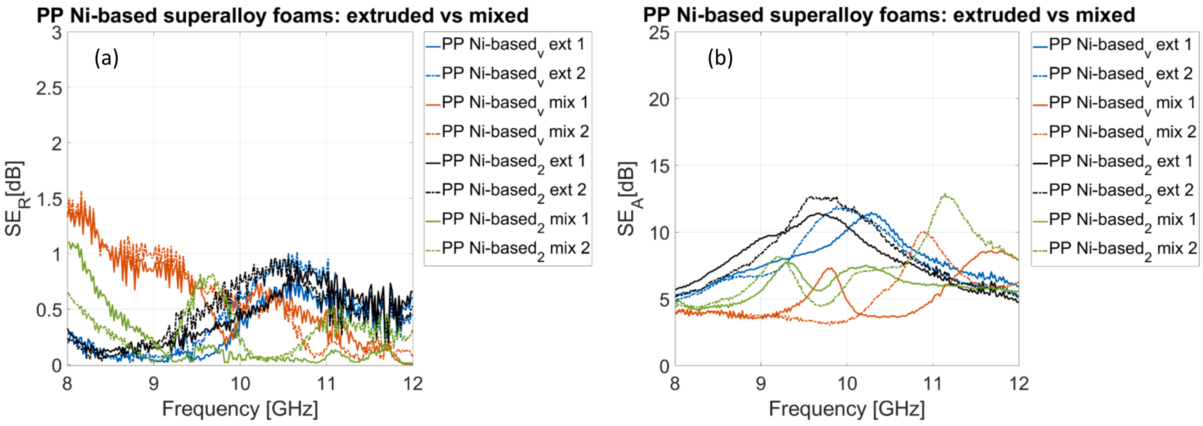

Fig. 15. (a) SE$_R$ and (b) SE$_A$ of foams obtained by extruded and mixed PP with virgin and reused (2 cycles) Ni Superalloy.

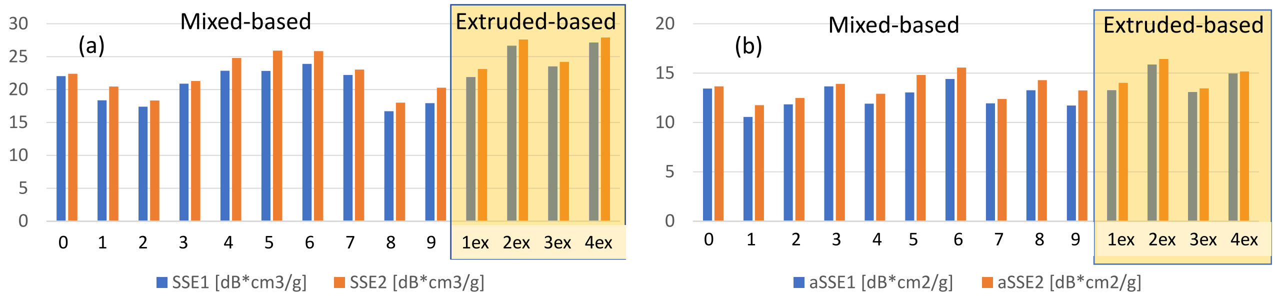

Fig. 16. (a) SSE and (b) aSSE for all measured samples.

6. Conclusions

The present study investigated the suitability of virgin and reused metal powders from PBF-LB and recycled PP foams for realizing microwave absorbers. All foams were produced using the chemical foaming process of polymeric pellets and metal powder or pellets of the composite material obtained via extrusion, adding 1 wt% ADC and setting the same process parameters (foaming temperature of 190°C and foaming time of 105 min).

SEM and EDS analyses were performed on metal powders, AISI 316 L and Ni-based superalloy types, to verify the elemental composition and oxidation. Subsequently, SEM acquisitions were carried out on foams that included the aforementioned powders to examine their distribution in the porous structures. A confocal microscope examined the morphology of the foams; the images were then post-processed with a visual software to evaluate the main morphological parameters – relative densities, cell numbers, areas, and distributions. The composition of the metal powder seems to be the most significant variable affecting the formation and size of the air cells during the foaming process. Their effect is probably ascribable to the peculiar nucleation ability, which depends on their thermal conductivities and how close they are to the thermal conductivity of the matrix. Overall, the virgin powder shows mainly a lower median cell area distribution and a slightly lower relative density than the reused powders, except for the most used powder, AISI316L, with 50 cycles, which showed, on the contrary, the lowest value. On average, all the fillers slightly increase the circularity of the cells. The powders do not significantly affect the cell density, except for AISI 316L, whose effect is also strongly dependent on the powder's quality (virgin and number of reuses), with an evident reduction of the cell density as the number of reuses increases.

To study the absorbance capability of the foams and assess the proper frequency range for the measurements, numerical analyses were performed on pure PP foams and PP foams filled with steel particles, having different distributions. The results showed that air cell areas, cell elongation, and distribution/location of metal particles impact the SE_A significantly, which is influenced by the combined effects of multiple internal reflections induced by air cells and scattering from metal particles. In contrast, SE_R is very low in the full frequency range, especially in the PP foam, which is more sensitive to the foam's effective permittivity and thickness, i.e., the relative density; conversely, SE_R increases when metal particles are introduced, due to enhanced reflection contribution of metal particles.

The X-band measurements confirmed the SE_R's numerical results, quite independently of foam morphology or metal powder type. At the same time, the measurements also show a significant variability of SE_A, especially depending on the sample morphology and orientation. In this regard, the samples with PP and virgin 17- 4PH, characterized by high relative density and very small air cell areas, exhibited high SE_A values (peaks of around 13–14 dB) in the X-band (15–25 dB). Conversely, PP samples with virgin AISI316L, WC/Co/Cr, and Ni-based superalloys, which feature low relative densities and the presence of large air cells, showed a lower SE_A performance compared to pure PP foam and also below the satisfactory range (10–13 dB). This discrepancy can be reasonably imputed to the impact of the thermal conductivity on the foam morphology and metal powders' electrical conductivity on the EM response. The reused metal powders show slightly higher SE_A peak values than the virgin ones. The differences observed in the EM response seem to be related to the morphology of the foam, and in the majority of the composites, the higher the value of the density, the higher the magnitude of the SE_A peaks, and the higher the cell area distribution median, the higher the wavelength of the peaks.

Finally, concerning the foams obtained from composite pellets, even though a better distribution of the metal powders in the PP matrix is visible also from SEM images, and affects the foam lightness, decreasing the relative density, the SE_A results did not significantly improve compared to the mixed samples. However, since all half samples did not have the same densities and thickness, the evaluation of SSE = avSE/ρ [dB/g/cm^3]) and Absolute Specific SE, aSSE=SSE/t [dB/g/cm^2] was carried out. The results demonstrated that all samples exhibited improved EMI shielding capability when oriented at 90° (direction 2); moreover, regarding the metal particle type and method used for metal particle inclusion in the PP matrix, extruded-based foams, especially concerning AISI316L 50 and Ni 2, showcased improved SSE and aSSE in the X-band compared to the mixed counterparts.

Although the obtained absorbance performance is not fully satisfactory, the proposed investigation proved that recycled PP and reused metal powders from PBF-LB could be suitable for producing EMI shielding foams, and future work will be aimed at optimizing the sample processes and morphology to attain higher SE_As in a larger frequency range, i.e., the X- and Ku-bands. In this regard, additional metal powder characterizations will also be scheduled for detailed insights into the thermal and electrical conductivity and their role in the process and SE performance.

CRediT authorship contribution statement

Valeria Marrocco: Writing – original draft, Validation, Methodology, Investigation, Formal analysis, Conceptualization. **Rossella Surace:** Writing – review & editing, Validation, Methodology, Investigation, Formal analysis, Conceptualization. **Elisabetta Brandonisio:** Investigation, Data curation. **Ilaria Marasco:** Software, Investigation. **Claudia Pagano:** Writing – review & editing, Investigation. **Cinzia Tonetti:** Investigation. **Vito Errico:** Investigation. **Giovanna Calò:** Supervision, Methodology. **Sabina L. Campanelli:** Supervision. **Irene Fassi:** Supervision, Project administration.

Declaration of competing interest

The authors declare that they have no known competing financial interests or personal relationships that could have appeared to influence the work reported in this paper.

Acknowledgments

This study was carried out within the MICS (Made in Italy—Circular and Sustainable) Extended Partnership and received funding from the European Union NextGenerationEU (Piano Nazionale di Ripresa e Resilienza (PNRR)—Missione 4 Componente 2, Investimento 1.3-D. D.1551.11-10-2022, PE00000004. It was also funded by the Programma Regionale RIPARTI POC PUGLIA FESR/FSE 2014/2020 – ManuReFoam Cod. 49894278". Special thanks to Dr. Fabrizio Silva for the extruded precursors.

Data availability

Data will be made available on request.

References

[1] A.K. Singh, A. Shishkin, T. Koppel, N. Gupta, Porous material for EMI shielding, in Materials for Potential EMI Shielding Applications, Ed. Elsevier (2020) pp. 287-314. doi: 10.1016/B978-0-12-817590-3.00018-X.

[2] Z. Sun, J. Yu, C. Liu, X. Jiang, X. Wang, Foam materials for applications of electromagnetic shielding and microwave absorption, Mater. Res. Bull. 180 (2024) 113001, https://doi.org/10.1016/j.materresbull.2024.113001.

[3] H. Yao, S. Kormakov, X. He, X. Gao, X. Zheng, Y. Liu, J. Sun, D. Wu, Conductive polymer composites from renewable resources: an overview of preparation, properties, and applications, Polymers 11 (2) (2019) 187, https://doi.org/10.3390/polym11020187Y.

[4] E. Mikinka, M. Siwak, Recent advances in electromagnetic interference shielding properties of carbon-fibre-reinforced polymer composites—a topical review, J. Mater. Sci. Mater. Electron. 32 (2021) 24585–24643, https://doi.org/10.1007/s10854-021-06900-8.

[5] M. Antunes, J.I. Velasco, Multifunctional polymer foams with carbon nanoparticles, Prog. Polym. Sci. 39 (3) (2014) 486–509, https://doi.org/10.1016/j.progpolymsci.2013.11.002.

[6] G. Wu, P. Xie, H. Yang, K. Dang, Y. Xu, M. Sain, L.S. Turng, W. Yang, A review of thermoplastic polymer foams for functional applications, J. Mater. Sci. 56 (2021) 11579–11604, https://doi.org/10.1007/s10853-021-06034-6T.

[7] Z. Standau, S. Chunjing, S. Murillo Castellón, C. Bonten, V. Altstädt, Chemical modification and foam processing of polylactide (PLA), Polymers 11 (2) (2019) 306, https://doi.org/10.3390/polym11020306.

[8] M. Hamidinejad, B. Zhao, A. Zandieh, N. Moghimian, T. Filleter, C.B. Park, Enhanced electrical and electromagnetic interference shielding properties of polymer graphene nanoplatelet composites fabricated via supercritical- fluid treatment and physical foaming, ACS Appl. Mater. Interfaces 10 (36) (2018) 30752–30761, https://doi.org/10.1021/acsami.8b10745.

[9] G. Wang, G. Zhao, S. Wang, L. Zhang, C.B. Park, Injection-molded microcellular PLA/graphite nanocomposites with dramatically enhanced mechanical and electrical properties for ultra-efficient EMI shielding applications, J. Mater. Chem. C 6 (25) (2018) 6847–6859, https://doi.org/10.1039/C8TC01326H.

[10] L. Wang, L.H. Wang, V. Mark, G. Shaayegan, H. Wang, G. Li, C.B. Zhao, Ultralow-threshold and lightweight biodegradable porous PLA/MWCNT with segregated conductive networks for high-performance thermal insulation and electromagnetic interference shielding applications, ACS Appl. Mater. Interfaces 10 (1) (2017) 1195–1203, https://doi.org/10.1021/acsami.7b14111.

[11] V. Marrocco, R. Surace, G. Calò, E. Brandonisio, I. Marasco, F. Filograno, I. Fassi, Chemical foaming of Carbon Fiber-Polylactic Acid (CF-PLA) porous structures and their feasibility as EMI shields in the X-band, IEEE Access 12, pp. 78110-78121, (2024) https://doi: 10.1109/ACCESS.2024.3407365.

[12] A. Bregman, E. Michielssen, A. Taub, Comparison of experimental and modeled EMI shielding properties of periodic porous xGNP/PLA composites, Polymers 11 (8) (2019) 1233, https://doi.org/10.3390/polym11081233.

[13] A. Ameli, P.U. Jung, C.B. Park, Electrical properties and electromagnetic interference shielding effectiveness of polypropylene/carbon fiber composite foams, Carbon 60 (2013) 3379–3391, https://doi.org/10.1016/j.carbon.2013.04.050.

[14] A. Kaushal, V. Singh, Analysis of mechanical, thermal, electrical and EMI shielding properties of graphite/carbon fiber reinforced polypropylene composites prepared via a twin screw extruder, Appl. Polym. Sci. 139 (1) (2022) e51444, https://doi.org/10.1002/app.51444.

[15] A. Ameli, M. Nofar, S. Wang, C.B. Park, Lightweight polypropylene/stainless-steel fiber composite foams with low percolation for efficient electromagnetic interference shielding, ACS Appl. Mater. Interfaces 6 (14) (2014) 11091, https://doi.org/10.1021/am500445g.

[16] A. Agrawal, A. Satapathy, Effects of aluminum nitride inclusions on thermal and electrical properties of epoxy and polypropylene: an experimental investigation, Compos. Part A-Appl. S 63 (2014) 51–58, https://doi.org/10.1016/j.compositesa.2014.04.001.

[17] Y. Zhou, J. Hu, X. Chen, F. Yu, J. He, Thermoplastic polypropylene/aluminum nitride nanocomposites with enhanced thermal conductivity and low dielectric loss, IEEE T Dielect El in 23 (5) (2016) 2768–2776, https://doi.org/10.1109/TDEI.2016.005994.

[18] K. Wilczyński, A. Wróblewska, A. Daniszewska, J. Krupka, M. Mrozowski, M. Zdrojek, Modulation of dielectric properties in low-loss polypropylene-based composites at GHz frequencies: theory and experiment, Sci. Rep. -UK 12 (2022) 13104, https://doi.org/10.1038/s41598-022-17173-4.

[19] C.W. Lee, C.H. Lin, L.Y. Wang, Y.H. Lee, Developing sustainable and recyclable high-efficiency electromagnetic interference shielding nanocomposite foams from the upcycling of recycled poly(ethylene terephthalate), Chem. Eng. J. 468 (2023) 143447, https://doi.org/10.1016/j.cej.2023.143447.

[20] M. Barclift, S. Joshi, T. Simpson, C. Dickman, Cost Modeling and Depreciation for Reused Powder Feedstocks in Powder Bed Fusion Additive Manufacturing, University of Texas at Austin, 2016.

[21] G. Jacob, C. Brown, A. Donmez, S. Watson, J. Slotwinski, Effects of powder recycling on stainless steel powder and built material properties in metal powder bed fusion processes, NIST.AMS 100–6 (2017), https://doi.org/10.6028/NIST.AMS.100-6.

[22] R. Surace, V. Errico, M. Valori, I. Fassi, S.L. Campanelli, Laser-powder bed fusion molds without post-processing for micro-injection molding of mini/micro-products, Int. J. Adv. Manuf. Technol. 127 (2023) 677–688, https://doi.org/10.1007/s00170-023-11585-w.

[23] L. Cordova, M. Campos, T. Tinga, Revealing the effects of powder reuse for selective laser melting by powder characterization, JOM 71 (2019) 1062–1072, https://doi.org/10.1007/s11837-018-3305-2.

[24] L.C. Ardila, F. Garciandia, J.B. González-Díaz, P. Álvarez, A. Echeverria, M. M. Petite, R. Deffley, J. Ochoa, Effect of IN718 recycled powder reuse on properties of parts manufactured by means of selective laser melting, Phys. Procedia 56 (2014) 99–107, https://doi.org/10.1016/j.phpro.2014.08.152.

[25] H.P. Tang, M. Qian, N. Liu, N.X.Z. Zhang, G.Y. Yang, J. Wang, Effect of powder reuse times on additive manufacturing of Ti-6Al-4V by selective electron beam melting, JOM 67 (2015) 555–563, https://doi.org/10.1007/s11837-015-1300-4.

[26] D. Powell, A.E.W. Rennie, L. Geekie, N. Burns, Understanding powder degradation in metal additive manufacturing to allow the upcycling of recycled powders, J. Clean. Prod. 268 (2020) 122077, https://doi.org/10.1016/j.jclepro.2020.122077.

[27] J.H. Warner, S.P. Ringer, G. Proust, Strategies for metallic powder reuse in powder bed fusion: a review, J. Manuf. Process. 110 (2024) 263–290, https://doi.org/10.1016/j.jmapro.2023.12.066.

[28] Z. Zhuo, R. Ji, L. Wang, J. Mao, Reusability of Ti-6Al-4V powder in laser powder bed fusion: Influence on powder morphology, oxygen uptake, and mechanical properties, J Mater Process Tech 335 (2025), https://doi.org/10.1016/j.jmatprotec.2024.118672.

[29] J. Li, W. Liu, J. Shen, X. Zhang, S. Li, Z. Wang, Research progress of the metal powder reuse for powder bed fusion additive manufacturing technology, Powder Technol. 441 (2024), https://doi.org/10.1016/j.powtec.2024.119815.

[30] P. Zapico, S. Giganto, J. Barreiro, S. Martínez-Pellitero, Characterisation of 17-4PH metallic powder recycling to optimise the performance of the selective laser melting process, J Mater Res Tech 9 (2) (2020) 1273–1285, https://doi.org/10.1016/j.jmrt.2019.11.054.

[31] M.J. Heiden, L.A. Deibler, J.M. Rodelas, J.R. Koepke, D.J. Tung, D.J. Saiz, B. H. Jared, Evolution of 316L stainless steel feedstock due to laser powder bed fusion process, Add Manuf 25 (2019) 84–103, https://doi.org/10.1016/j.addma.2018.10.019.

[32] V. Errico, A. Fusco, S.L. Campanelli, Effect of DED coating and DED + laser scanning on surface performance of L-PBF stainless steel parts, Surf and Coatings Technol 429 (2022) 127965, https://doi.org/10.1016/j.surfcoat.2021.127965.

[33] X. Li, M. Zhou, S. Peng, X. Chen, X. Ge, B. Huang, L. Cui, S. Hao, Revealing effects of powder reuse for LPBF-fabricated NiTi shape memory alloys, Front. Mater. Sci. 18 (2024) 240697, https://doi.org/10.1007/s11706-024-0697-5.

[34] J.H. Warner, et al., Strategies for metallic powder reuse in powder bed fusion: a review, J. Manuf. Process. 110 (2024) 263–290.

[35] R.L. Guo, S.H. Liu, Y.M. Lu, Investigation of how pressure influences the thermal decomposition behavior of azodicarbonamide, J. Loss Prev. Process Ind. 83 (2023) (2023) 105062, https://doi.org/10.1016/j.jlp.2023.105062.

[36] C.B. Park, L.K. Cheung, A study of cell nucleation in the extrusion of polypropylene foams, Polym. Eng. Sci. 37 (1) (1997), https://doi.org/10.1002/pen.11639.

[37] Q.B. Ho, M. Kontopoulou, Stabilization of the cellular structure of polypropylene foams and secondary nucleation mechanism in the presence of graphene nanoplatelets, Polymer 198 (2020), https://doi.org/10.1016/j.polymer.2020.122506.

[38] J. Xing, J. Gu, B. Liu, L. He, T. Jiang, Fabrication of lightweight, tough polypropylene composite foams: effects of nucleating agent structure on the foaming behavior and tensile property of polypropylene foams, J. Polym. Res. 31 (2024) 142, https://doi.org/10.1007/s10965-024-03978-6.

[39] Y. Xu, X. Wang, Q. Hao, A mini review on thermally conductive polymers and polymer-based composites, Composites Commun 24 (2021) 100617, https://doi.org/10.1016/j.coco.2020.100617.

[40] Y.P. Mamunya, V.V. Davydenko, P. Pissis, E.V. Lebedev, Electrical and thermal conductivity of polymers filled with metal powders, Eur. Polym. J. 38 (9) (2002) 1887–1897, https://doi.org/10.1016/S0014-3057(02)00064-2.

[41] I.L. Ngo, S. Jeon, C. Byon, Thermal conductivity of transparent and flexible polymers containing fillers: a literature review, Int J Heat Mass Tran 98 (2016) 219–226, https://doi.org/10.1016/j.ijheatmasstransfer.2016.02.082.

[42] H. Chen, V.V. Ginzburg, J. Yang, Y. Yang, W. Liu, Y. Huang, L. Du, B. Chen, Thermal conductivity of polymer-based composites: fundamentals and applications, Prog. Polym. Sci. 59 (2016) 41–85, https://doi.org/10.1016/j.progpolymsci.2016.03.001.

[43] Y. Yao, S. Jin, H. Zou, L. Li, X. Ma, G. Lv, F. Gao, X. Lv, Q. Shu, Polymer-based lightweight materials for electromagnetic interference shielding: a review, J. Mater. Sci. 56 (2021) 6549–6580, https://doi.org/10.1007/s10853-020-05635-x.

[44] A.M. Helmenstine, Table of electrical resistivity and conductivity, Science, Tech, Math (2019) https://www.thoughtco.com/table-of-electrical-resistivity-conductivity-608499.

[45] K.L. Zhang, Z.L. Hou, L.B. Kong, H.M. Fang, K.T. Zhan, Origin of negative imaginary part of effective permittivity of passive materials, Chin. Phys. Lett. 34 (9) (2017), https://doi.org/10.1088/0256-307X/34/9/097701.